國 立 交 通 大 學

電子工程學系電子研究所

碩 士 論 文

利用通道背向散射理論及溫度係數模型分析奈米
級金氧半電晶體電子遷移率的劣化之研究

Analysis of Mobility Degradation in Nanoscale DG nMOSFETs Using Channel Backscattering Theory and Temperature Coefficient Method

研 究 生：詹益先　　Yi-Hsien Chan

指導教授：陳明哲　　Prof. Ming-Jer Chen

中 華 民 國 九 十 九 年 九 月

利用通道背向散射理論及溫度係數模型分析奈米級金氧半電晶體電子遷移率的劣化之研究

Analysis of Mobility Degradation in Nanoscale DG nMOSFETs Using Channel Backscattering Theory and Temperature Coefficient Method

研 究 生: 詹益先   Student: Yi-Hsien Chan

指導教授: 陳明哲   Advisor: Ming-Jer Chen

國 立 交 通 大 學

電子工程學系 電子研究所

碩 士 論 文

A Thesis

Submitted to Department of Electronics Engineering & Institute of Electronics

College of Electrical and Computer Engineering

National Chiao Tung University

in Partial Fulfillment of the requirements

for the Degree of Master

in

Electronic Engineering

September 2010

Hsinchu, Taiwan, Republic of China

中華民國九十九年九月

利用通道背向散射理論及溫度係數模型分析奈米級金氧半電晶體電子遷移率的劣化之研究

研究生: 詹益先　　　　　　　　　　　指導教授: 陳明哲博士

國立交通大學

電子工程學系電子研究所

摘要

近年來許多的研究指出，當金氧半場效電晶體的元件尺寸縮減到數百奈米至數十奈米時，電子遷移率將隨通道長度減少而遞減。研究指出此電子遷移率的降低是因為載子在元件中有其所對應的飽和速度，其載子將無法超越此一速度。所以此篇論文主旨在於探討當元件尺寸縮減時，將面臨平衡態區域範圍的縮減。因此我們利用的模擬軟體 TCAD 模擬奈米級雙閘極電晶體的特性，其中我們考慮了擴散飄移模型以及量子效應。在此我們為了獲得其不受飽和速度影響的電子遷移率，必須要在極小的汲極偏壓下模擬。除此之外利用通道背向散射理論來解釋其飽和速度的現象，並且利用其隨溫度變化的特性來加以分析。最後比較模擬的臨界散射長度以及計算值間的差異性，加以修正而得其合理之結果。

Analysis of Mobility Degradation in Nanoscale DG nMOSFETs Using Channel Backscattering Theory and Temperature Coefficient Method

Student: Yi-Hsien Chan   Advisor: Dr. Ming-Jer Chen

Department of Electronics Engineering

Institute of Electronics

National Chiao Tung University

Abstract

In recent years, many investigations point out that mobility would degrade with the channel length scaling down in nanoscale MOSFETs. It is suggested that the reason for the mobility degradation is caused by the corresponding saturation velocity. The carrier velocity cannot excess this limit in nature. Therefore, we focus on the exploration of the mobility decrease in drain current linear region with channel length shrinkage. First, we simulate the DG nMOSFET characteristics by using TCAD simulator. In the simulation, we consider the drift-diffusion model and quantum effect. In order to extract the real mobility at equilibrium condition, we simulate the case at $V_D=1mV$. Furthermore, we use the channel backscattering theory to explain the effect of saturation velocity and use the temperature coefficient method to analyze the variation between the two methods. Finally, we compare the error of the critical scattering length between the simulation result and the calculation result, along with the correction to get a feasible result.
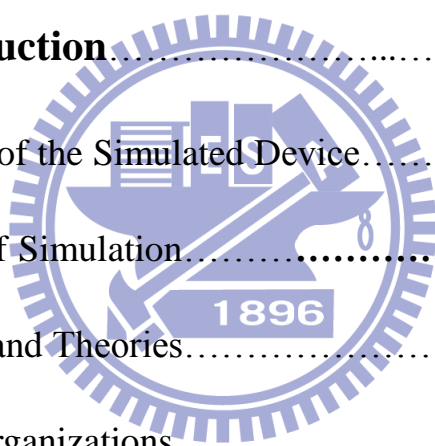
誌 謝

在我就讀碩士班的這兩年來，雖不可稱得上一帆風順，但在陳明哲老師的指導下，讓我順利低完成碩士學業。在此感謝陳明哲老師孜孜不倦的指導，並且提供良好的研究環境與資源，讓我收穫頗多。此外，感謝謝振宇、李建志、許智育以及李韋漢學長們總是親切低在這兩年來提供各方面的協助與指導，以及湯侑穎學長與我共同奮鬥了一年。也謝謝蔡濬澤、鄭寬豪與張華罡三位同學與我在老師的帶領下互相勉勵，學習成長，一起度過了很多在實驗室趕進度挑燈夜戰的時光。實驗室的學弟妹也在平常提供了不少協助，並帶給實驗室很多活力與歡樂。特別要感謝光心君學妹與彭霖祥學弟，在研究上對我幫助良多。最後要感謝我的父母朋友們，作為我的後盾以及支柱，讓我能無後顧之憂的完成碩士學業。最後謝謝口試委員(林鴻志教授以及張智勝博士)所給予的寶貴意見，讓我完成一份更好的論文。

2010 年 9 月

詹益先

Contents

List of Captions

List of Symbols

Symbol	Meaning
L_{kT}	critical scattering length
x_{vs}	virtual source position
F^+	injection flux from source to channel
F_b^-	injection flux from drain to source
T^+	transmission coefficient for F^+ flux
T^-	transmission coefficient for F_b^- flux
Q_{inv}	inversion charge density
N_{inv}	inversion carrier density
v_T	equilibrium unidirectional thermal velocity
v_{inj}	injection velocity
R_S	series resistance at source
R_D	series resistance at drain
λ	mean free path
μ_0	mobility at equilibrium
r_c	scattering coefficient
BR	ballistic ratio
n_{vi}	degeneracy factor of ith valley
m_{di}	density of states effective mass of ith valley
E_f	quasi-Fermi level
Φ_n	electron quasi-Fermi potential function
Φ_p	hole quasi-Fermi potential function
γ_{Lkt}	temperature coefficient of L_{kT}
γ_μ	temperature coefficient of μ_0
$\gamma_{\upsilon_{inj}}$	temperature coefficient of v_{inj}
α	temperature coefficient of drain current
β	temperature coefficient of inversion carrier density

Chapter 1

Introduction

Section 1.1 Structure of the Simulated Device

In this simulation, we explore the 2-D double gate n-channel MOSFETs, which were simulated by using the TCAD (Sentaurus) simulator. The simulated devices have four channel length sizes from 90nm to 15nm, drain and source lengths are fixed at 20nm, oxide thickness is 6nm, body thickness is 6nm, poly gate doping concentration is 10^{20} cm^{-3} and body doping concentration is 3×10^{16} cm^{-3}. The simulation bias conditions are: V_G=0.8V; V_D=0.001V, 0.025V and 1V; and the operating temperature = 250K, 300K and 350K. Fig. 1-1 shows the structure of the simulated device. Metal contacts were set on the left end side of source, the right end side of drain, the upper end of gate, and the bottom end of gate. This forced us to consider the series resistances of highly-doped source and drain region. Since the contact is set as the ohmic contact. Therefore, the contact resistance is neglected.

Section 1.2 Models of Simulation

Usually, doing 2-D simulations would only use drift-diffusion model (DD model). DD model is not suited to analyze SOI structure and short channel structure. Therefore, the accurate prediction of the electrical characteristics of state-of-the-art nanoscale semiconductor devices

demands for the inclusion of quantum effects: this effect may cause increased equivalent oxide thickness due to strong electron confinement at Si/SiO2 interface. Some groups have proposed some complicated models or simulated the device at atomic level with Monte Carlo technique. Therefore, in order to get more accurate result in this simulation, we not only used the DD transport model but also appended 1-D Schrödinger–Poisson to confine the y-direction in the channel. The model is so called Schrödinger–Poisson–Drift–Diffusion (SPDD) model proposed in [1]. This gives us a relative correct solution of the analysis on channel status, for instance, sub-threshold swing, energy, and carrier density distribution along the channel. Furthermore, there are three mobility models that can be used to solve the DD transport model: (i) doping dependent mobility; (ii) high-field saturation [4]; and (iii) mobility degradation at interfaces (Enhanced Lombardi Model). The three models are combined by following Mathiessen's rule. The simulation model (ii) would be used to explain the characteristics of mobility degradation with channel length shrinkage in Chapter 3.

Section 1.3 Analysis and Theories

With channel length decreasing to nanoscale, the most important issue we faced is the high field saturation. Fortunately, there is two models proposed to explain the effect: (i) the traditional model called Caughey-Thomas formula [4] suitable to analyze the status along the channel; and (ii) channel backscattering theory proposed by Lundstrom, *et al*. [2]. By the theory, the barrier position of the lowest sub-band

energy called the virtual source point X_{vs} dominates device characteristic and the critical scattering length. Fig. 1-2 shows a schematic diagram of channel backscattering theory. The status at X_{vs} can critically determine the device performance. Using the theory, it can help us analyze the effect of mobility degradation and backscattering flux degradation in the scaling direction.

Section 1.4   Thesis Organizations

In this thesis, we explore the phenomenon of mobility degradation and the possibility of applying the channel backscattering theory to the result simulated by traditional transport model with channel scaling down at three different temperatures. The following Chapter 2 will explain the channel backscattering theory and the temperature coefficient method proposed elsewhere [3]. And in Chapter 3, we will show the simulation result and extract the temperature coefficients. Furthermore, we will give the reasons of mobility degradation and compare the errors between the channel backscattering theory and temperature coefficient method. We also will bring up a possible solution to make us the extracted ballistic ratio proper. Finally, we make a conclusion in Chapter 4.

Chapter 2

Channel Backscattering Theory

Section 2.1 Introduction

Channel backscattering theory is a simple one-flux scattering theory used in MOSFETs [2], [10], [11], [12]. The theory gives a new expression of current-voltage characteristics used to analyze short-channel devices. The new formula is expressed in terms of scattering parameters rather than a mobility. For long-channel transistors, the results reduce to conventional drift-diffusion (DD) theory. But DD theory also applies to short channel device even as the channel length is shorter than the mean-free-path. In backscattering theory, the transconductance is limited by carrier injection from the source for ultra short channel. Another channel backscattering concept to analyze short channel effect has been proposed by [3] in terms of the Temperature Coefficient Method. In this concept, temperature is used to analyze the variation of channel status for different temperatures. By extracting the mean free path, critical scattering length, the temperature coefficients of mobility, injection velocity and the power law coefficients to define the ballistic ratio.

Section 2.2 Channel Backscattering Theory

With channel scaling down, traditional current model would touch a limit caused by the saturation velocity. The key issue of channel backscattering theory is to maximize the saturation drain current for

short-channel devices. Electrons are injected from the source into the channel across a potential barrier varying with the gate voltage and the drain voltage. Traditionally, carriers drift and diffuse across the channel and finally are collected at the drain. Fortunately, TCAD can work well on the 2D simulation. That is we could simply grasp the status on the virtual source point. And drain-induced barrier lowering (DIBL) has been taken into account by using TCAD simulator. In the theory, the virtual source at the barrier height is considered as a carrier reservoir; which injects a flux from the source side across the barrier into the channel. There are not all of the carriers that can transmit across the barrier. A fraction of the flux, r_c, goes back to the source. The backscattering region, k-T layer, is the key region which dominates the backscatter flux. As shown in Fig. 1-2, k-T layer is the length from the barrier height to the point with a kT potential drop rather than the barrier point. The length is called critical scattering length, L_{kT}. Physically, the channel length is equal to the critical scattering length at very small drain bias. Therefore, whenever the critical length is larger than the channel length, L_{kT} is assumed to be the same as L_G. We can find the corresponding drain current from the backscattering coefficient r_c as below. In Fig. 1-2, F^+ is the injection flux from source to channel, and F_b^- is the injection flux from drain to source. T^+ is the transmission coefficient for F^+ flux, and T^- is the transmission coefficient for F_b^- flux. At equilibrium, T^- approximates $T^+=T$,

$$I_{DS}/W = q(F^+(0) - F^-(0)), \tag{2-1}$$

$$Q_{inv}(0) = q(F^+(0) + F^-(0))/\upsilon_T, \tag{2-2}$$

where υ_T is the equilibrium unidirectional thermal velocity (i.e., the average velocity of carrier across the barrier in the positive direction). And position 0 is defined at the X_{vs} point. From Eq. (2-1) and (2-2), the drain current can be expressed as:

$$\frac{I_{DS}}{W} = Q_{inv}(0)\upsilon_T \frac{1-\frac{F^-(0)}{F^+(0)}}{1+\frac{F^-(0)}{F^+(0)}}. \qquad (2\text{-}3)$$

Under ballistic condition, the negative flux caused by thermal emission from the drain is given by thermionic emission as:

$$F_b{}^-(0) = F^+(0)e^{-qV_{DS}/k_bT}, \qquad (2\text{-}4)$$

$$F^-(0) = (1-T)F^+(0) + TF_b{}^-(0), \text{where } T = T^+ = T^-. \qquad (2\text{-}5)$$

Substituting Eq. (2-4) and (2-5) into (2-3), we have

$$\frac{I_{DS}}{W} = Q_{inv}(0)\upsilon_T \frac{1-r_c}{1+r_c}\frac{1-e^{-qV_{DS}/k_bT}}{1+\frac{1-r_c}{1+r_c}e^{-qV_{DS}/k_bT}}, \text{where } r_c = 1-T. \qquad (2\text{-}6)$$

And taking the series resistance effect into Eq. (2-6), we can get the drain current at linear and saturation regions:

$$I_{DS,sat}/W = Q_{inv}(0)\upsilon_{ox}, \text{where } \upsilon_{ox} = \upsilon_T\frac{1-r_c}{1+r_c}, \qquad (2\text{-}7)$$

$$I_{DS,lin}/W = Q_{inv}(0)\upsilon_T(1-r_c)\frac{q(V_{DS}-I_{DS,lin}(R_s+R_d))}{2k_bT}, \qquad (2\text{-}8)$$

where $Q_{inv}(0)$ is the inversion carrier density per unit area at virtual source, X_{vs}, point and R_S/ R_D are the series resistance at the source/ drain. $\upsilon_T = \sqrt{2k_bT/\pi m^*}$ is the thermal velocity for nondegenerate case. For the degenerate case, we use the injection velocity to replace the thermal

velocity. The injection velocity can be expressed as $\upsilon_{inj} = \upsilon_T \frac{\mathfrak{I}_{1/2}(\eta_F)}{\mathfrak{I}_0(\eta_F)}$. Furthermore, r_c can be expressed as:

$$r_c = \frac{L_{kT}}{L_{kT}+\lambda}, \text{ where } \lambda = \frac{2kT\mu_0}{\upsilon_T}\frac{\mathfrak{I}_0(\eta_F)}{\mathfrak{I}_{-1}(\eta_F)}, \tag{2-9}$$

λ is the mean free path and μ_0 is the mobility extracted at thermal equilibrium. In simulation, DIBL has been included. Therefore, Q_{inv} has DIBL effect in itself.

Section 2.3 Mean Free Path and Critical Scattering Length

The mean free path is a controlling factor to determine the performance of device. It is associated with the mobility and the thermal injection velocity. Besides, the critical scattering length is widely evaluated by each group's study [5], [6], [14]; that is, how to calculate L_{kT} would really decide the characteristics of device. Therefore, we will slightly correct the critical scattering length by using the direct extraction of L_{kT} from the simulation result.

Section 2.4 Temperature Coefficient Method (TC Model)

In section 2.2, we explained the component of the backscattering coefficient, r_c. It can be clearly found that it has some relationship with the temperature. This means there is another way to extract the scattering coefficient r_c. This is TC model. Replacing r_c with λ and L_{kT}, leading to

$$I_{D,sat}/W = Q_{inv}\upsilon_{inj}\frac{\lambda/L_{kT}}{2+\lambda/L_{kT}}. \tag{2-10}$$

To accommodate Eq. (2-10), the power law relationships of each parameter shown in below:

$$\upsilon_{inj} \propto T^{\gamma_{\upsilon_{inj}}}; \quad \mu_0 \propto T^{\gamma_\mu};$$

$$\rightarrow \lambda = \frac{2kT\mu_0}{\upsilon_{inj}} \propto C_1 T^{1+\gamma_\mu - \gamma_{\upsilon_{inj}}}.$$

$$L_{kT} \propto C_2 T^{\gamma_{Lkt}};$$

$$\rightarrow \frac{1-r_c}{1+r_c} = \frac{\lambda/L_{kT}}{2+\lambda/L_{kT}} \propto \frac{C_1 T^{1+\gamma_\mu - \gamma_{\upsilon_{inj}}}}{2C_2 T^{\gamma_{Lkt}} + C_1 T^{1+\gamma_\mu - \gamma_{\upsilon_{inj}}}}. \tag{2-11}$$

Differentiating Eq. (2-5) with respect to temperature:

$$\frac{\partial(\frac{\lambda}{2L_{kT}+\lambda})}{\partial T} = \frac{\partial(\frac{C_1 T^{1+\gamma_\mu - \gamma_{\upsilon_{inj}}}}{2C_2 T^{\gamma_{Lkt}} + C_1 T^{1+\gamma_\mu - \gamma_{\upsilon_{inj}}}})}{\partial T}$$

$$= \frac{2C_1 C_2 T^{\gamma_{Lkt}+\gamma_\mu - \gamma_{\upsilon_{inj}}}}{(2C_2 T^{\gamma_{Lkt}} + C_1 T^{1+\gamma_\mu - \gamma_{\upsilon_{inj}}})^2} C_3, \tag{2-12}$$

where $C_3 = (1 - \gamma_{Lkt} + \gamma_\mu - \gamma_{\upsilon inj})$. Again differentiating Eq. (2-10) with respect to temperature,

$$\frac{\partial I_D/W}{\partial T} = \upsilon_{inj} \frac{\lambda}{L_{kT}+\lambda} \frac{\partial Q_{inv}}{\partial T} + Q_{inv} \frac{\lambda}{L_{kT}+\lambda} \frac{\partial \upsilon_{inj}}{\partial T} + Q_{inv}\upsilon_{inj} \frac{\partial \frac{\lambda}{L_{kT}+\lambda}}{\partial T}; \tag{2-13}$$

$$Q_{inv} \propto T^\beta; \quad I_D \propto T^\alpha;$$

$$\frac{\partial I_D}{I_D \partial T} = \frac{1}{Q_{inv}} \frac{\partial Q_{inv}}{\partial T} + \frac{1}{\upsilon_{inj}} \frac{\partial \upsilon_{inj}}{\partial T} + \frac{1}{\frac{\lambda}{L_{kT}+\lambda}} \frac{\partial \frac{\lambda}{L_{kT}+\lambda}}{\partial T}. \tag{2-14}$$

Substituting Eq. (2-12) into (2-14),

$$\frac{\partial I_D}{I_D \partial T} = \frac{\alpha}{T} = \frac{\beta}{T} + \frac{\gamma_{\upsilon_{inj}}}{T} + \frac{2(1-\gamma_{Lkt}+\gamma_\mu - \gamma_{\upsilon_{inj}})}{T(2+\lambda/L_{kT})};$$

$$\rightarrow \frac{\lambda}{L_{kT}} = -2 + \frac{2(1-\gamma_{Lkt}+\gamma_\mu - \gamma_{\upsilon_{inj}})}{\alpha-\beta-\gamma_{Vinj}}. \tag{2-15}$$

Again substituting Eq. (2-15) into (2-11),

$$BR_{TC} = \frac{1-r_c}{1+r_c} = \frac{\lambda/L_{kT}}{2+\lambda/L_{kT}} = \frac{1-\gamma_{Lkt}+\gamma_{\mu-(\alpha-\beta)}}{1-\gamma_{Lkt}+\gamma_\mu - \gamma_{\upsilon_{inj}}}. \tag{2-16}$$

This is the temperature coefficient method to extract the ballistic ratio RB

and the scattering coefficient r_c.

Section 2.5 Conclusion

From Eq. (2-7), we can get BR directly and compare it with the result of TC model by using Eq. (2-16). Generally, the two methods may not get the same BR value for any conditions, but it would suggest that there is another factor needed to add into the simulation or the theory should be corrected. In Chapter 3, we will show the calculated result between the two methods.
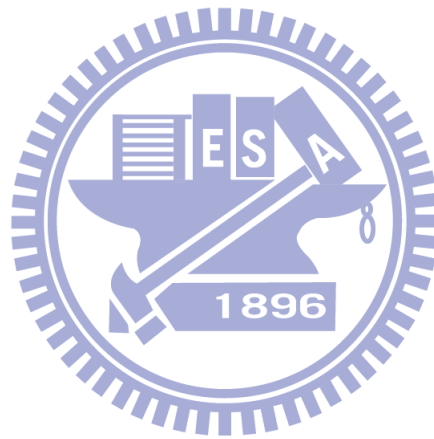
Chapter 3

Analysis of TCAD simulation result

Section 3.1 Introduction

In this chapter, we focus on: (i) the extraction of five power-law parameters (γ_{Lkt}, γ_μ, γ_{Vinj}, α, β); (ii) the extraction of BR; (iii) the comparison of BR between the direct extraction and the calculation result by using TC model; and (iv) the difference between the key point, $X=X_{vs}$, and the balance point, $X=0$. In the study, the whole channel status is taken into consideration by using the TCAD simulator. We used the quantum mechanics to accurately deal with the sub-band energy in the y direction along the channel, and drift and diffusion transport model to get a self-consistent solution along the channel.

Section 3.2 Extraction of Five Temperature Coefficients
Section 3.2.1 Schrödinger–Poisson–Drift–Diffusion (SPDD) model

The SPDD model was proposed in [1], [2]. From Schrödinger equation (3-1), a set of quantum energy states $\{Eij\}$, i, $j \in \mathbb{N}$, can be solved:

$$\nabla\left(\frac{-\hbar^2}{2m}\nabla\psi(x,y)\right) + E_c(x,y)\psi(x,y) = E_{ij}(x)\psi(x,y). \qquad (3\text{-}1)$$

With device parameters and the operation temperature and applied bias as input, TCAD can accurately calculate the sub-band energy and the

Fermi-level, thus producing the inversion layer carrier density (2DEG) per sub-band as:

$$N_{ij}(x) = \left(\frac{-n_{vi}m_{di}k_bT}{\pi\hbar^2}\right)\ln\left(1 + \exp\left(\frac{E_f(x)-E_{ij}(x)}{k_bT}\right)\right), \qquad (3\text{-}2)$$

where i=1, 2 (valley), j=1, 2, 3 (sub-band)...; n_{vi} is the degeneracy factor of ith valley; m_{di} is the density of states effective mass of ith valley. E_f is the quasi-Fermi level.

And by using the Poisson equation as Eq. (3-3), we can get a self-consistent result of the Schrödinger–Poisson as shown in Fig. 3-1:

$$\nabla^2 E_c(x,y) = -\frac{\rho(x,y)}{\varepsilon_{si}} = \frac{q\sum_{ij}(N_{ij}(x)|\psi_{ij}(x,y)|^2)+\rho_{depl}(x,y)}{\varepsilon_{si}}. \qquad (3\text{-}3)$$

We get the 1-D Schrödinger–Poisson solution in the y-direction, and we can apply it to 2-D case by appending the DD model to constitute a self-consistent solution along the two directions as shown in Fig. 3-2. The electron and hole continuity equations are written as:

$$\nabla \cdot \overrightarrow{J_n} = qR_{net} + q\frac{\partial n}{\partial t}; \qquad (3\text{-}4)$$

$$-\nabla \cdot \overrightarrow{J_p} = qR_{net} + q\frac{\partial p}{\partial t}, \qquad (3\text{-}5)$$

where R_{net} is the net electron/ hole recombination rate, $\overrightarrow{J_n}$ is the electron current density, and $\overrightarrow{J_p}$ is the hole current density.

The DD model is widely used as a carrier transport model in semiconductors and is defined by the following equations for the current densities of electrons and holes:

$$J_n = -nq\mu_n\nabla\Phi_n; \qquad (3\text{-}6)$$

$$J_p = -pq\mu_p\nabla\Phi_p, \qquad (3\text{-}7)$$

where μ_n and μ_p are the electron and hole mobilities, and Φ_n and Φ_p are the electron and hole quasi-Fermi potentials, respectively.

Section 3.2.2 Channel Status at Equilibrium

Usually we thought the highest energy of conduction band would locate at the mid of channel, but it would vary from the mid of channel toward the source and drain with increasing gate voltage. As shown in Fig. 3-3 is a profile of the lowest sub-band, E_{11}, along the channel. We found the highest energy is located 2~5nm away from the junction of source/channel and channel/drain in channel. Fig. 3-4 show the sheet charge. In basic Poisson equation, we considered only forward or backward direction. In reality, we should take both into consideration. This leads to the result of Fig. 3-3. Apparently, the highest point of E_{11} is not located at the mid-channel. The difference between V_D=0V and 1mV is due to the variation of Fermi-Level.

The local higher potential causes a relative lower carrier density at that region. As shown in Fig. 3-5 is the inversion carrier density N_{inv} along the channel. We get almost the same N_{inv} at V_D=0V and 1mV. This shows channel is at equilibrium condition for V_D=1mV. Furthermore, we find that the inversion carrier density can be gradually affected as the channel length is scaled down. The effect of drain induced barrier lowering, DIBL, can cause the carrier density increasing for L_G=15nm, except at L_G=90nm. It shows a similar characteristic as [13]. The short channel effect would appear for channel length is smaller than 40nm or the temperature of 150K.

Finally, we want to compare how much difference between each channel length different gate voltages can produce. Here, we used a quite correct simulator, Schred [7], evaluated by Prof. Lundstrom, *et al.* at Purdue University, as the standard to check and analyze the TCAD's simulation result. As shown in Fig. 3-6-1, we can get a perfect match between TCAD and Schred at long channel, but source and drain affect the channel as channel scaling to 15nm. Usually, we think DIBL is a constant for sub-threshold and above threshold region. Indeed, the channel resistance is high below the sub-threshold region; and above threshold region, the source and drain resistance are relative higher. Therefore, DIBL is not a constant for any gate voltage as shown in Fig. 3-6-2.

Section 3.2.3 Mobility Extraction at Equilibrium

After analyzing the status of channel at equilibrium, it provided two ways to calculate the mobility for us. First, according to the experimental concept, using the results of I_D against V_G and the inversion carrier density calculated by C-V measurement, we should assume that the drain current uniformly flows through the channel and the carrier uniformly distributes in channel. The results are shown in Eq. (3-8). Second, according to the ballistic theory, carriers come from the virtual source and may be reflected with a critical scattering length L_{kt} and a mean free path λ. Whatever the methods used, it should follow the DD model as Eq. (3-6) and (3-7). As shown in equation (3-8), we can get a relationship between I_D per unit width and current density of electrons and holes. We can even reduce Eq. (3-8) to Eq. (3-9), because the majority carriers are electrons:

$$\frac{I_D}{W} = \int (J_n + J_p) dy$$

$$= -Q_n(x)\mu_n(x)\nabla\Phi_n(x) - Q_p(x)\mu_p(x)\nabla\Phi_p(x); \qquad (3\text{-}8)$$

$$\frac{I_D}{W} = -Q_{inv}(x)\mu_{app}(x)\nabla\Phi_n(x). \qquad (3\text{-}9)$$

Although the drain current is conserved along the channel, we can clearly find that from Fig. 3-5 the carrier density is not the same along the channel. From electron quasi Fermi-level along the channel as shown in Fig. 3-7, we can extract the series resistances of source and drain as shown in Fig. 3-8-1 and Fig. 3-8-2:

$$R_{tot} = \frac{V_D}{I_D} = \frac{\Delta V_{SD} + \Delta V_{Channel}}{I_D} = R_{SD} + R_{Channel}. \qquad (3\text{-}10)$$

Fig. 3-8-1, 3-8-2 and 3-8-3 show R_{tot}, R_{SD} and $R_{Channel}$, respectively, for four different channel lengths from 90nm to 15nm and three temperatures. There is a slight difference between two applied V_D, which is caused by the mobility degradation at $V_D=0.025V$. That suggests that it is not appropriate to extract mobility at drain bias of 0.025V for nanoscale device. We could predict the trend of mobility by using the characteristic of the channel resistance that is proportional to $1/L_G$ as revealed by Eq. (3-11). However, $R_{Channel}$ is not zero at $L_G=0$nm at all for $V_D=0.025V$:

$$R_{Channel} = \frac{\Delta V_{Channel}}{I_D} = \frac{L_G}{WQ_{inv}\mu_{app}} = \frac{L_G + \lambda}{WQ_{inv}\mu_{low}}; \qquad (3\text{-}11)$$

$$\mu_{app}(x) = \frac{I_D}{WQ_{inv}(x)\nabla\Phi_n(x)}, \qquad (3\text{-}12)$$

where $\mu_{app}(x)$ is the apparent mobility, μ_{low} is the low field mobility, and λ is a correction term due to the mobility degradation.

In Fig. 3-9-1, 3-9-2 and 3-9-3, we sight on the mid-channel (X=0) and $X=X_{vs}$. When V_D is 1mV, there is no decrease on mobility with the channel length, but we can find a strong degradation on mobility at V_D=25mV. This suggests the decrease of mobility with scaling down is caused by the saturation velocity. According to the Canali model evaluated by Canali *et al*. [4], it is used to explain the high field saturation phenomenon. The Caughey-Thomas formula is shown in below:

$$\mu_{app}\big(\nabla\Phi_f(x)\big) = \frac{\mu_{low}}{\left(1+\left(\frac{\mu_{low}\nabla\Phi_f(x)}{\upsilon_{sat}}\right)^{\beta}\right)^{1/\beta}}; \tag{3-13}$$

$$\beta = \beta(\frac{T}{300})^{\beta exp};$$

$$\upsilon_{sat} = \upsilon_{sat,0}(\frac{300}{T})^{\upsilon_{sat,exp}};$$

where υ_{sat} is the saturation velocity and β is a fitting parameter for Caughey-Thomas formula. Parameters' setting is shown in Table 1. We confirmed the mobility degradation by using the Caughey-Thomas formula. As shown in Fig. 3-9-4, we set the low field mobility the same as the mobility extracted from DD model at V_D=1mV and L_G=90nm. The result agrees with our prediction. That is the mobility degradation caused by the limit of saturation velocity with channel length shrinkage.

Section 3.2.4 Critical Scattering Length L_{kT} Extraction in Saturation Region (V_G=0.8V and V_D=1V)

Within the framework of the channel backscattering theory, carrier will be scattered in the k-T layer. As the drain voltage is smaller than the thermal energy, the critical scattering length must be equal to the channel length. That explains why we should extract L_{kT} in the saturation region.

L_{kT} is expressed as:

$$L_{kT} \propto C_2 T^{\gamma_{Lkt}},$$ (3-14)

where C_2 and γ_{Lkt} are taken as parameters that can fit the simulation result. Generally, we extract L_{kT} from the conduction band energy profile $E_c(x, y)$. But $E_c(x, y)$ would vary with x and y direction. Therefore, we used the lowest sub-band energy profile $E_{11}(x)$ along the channel to substitute $E_c(x, y)$. As shown in Fig. 3-10-1, L_{kT} increases with increasing channel length and increasing temperature. Fig. 3-10-2 shows the extracted L_{kT} and the temperature coefficient for each channel length and temperature. It has the similar trend with Zilli, *et al.* [9]

Section 3.2.5 Injection velocity v_{inj} Extraction in Saturation Region (V_G=0.8V and V_D=1V)

Within the framework of the channel backscattering theory, carriers come from the virtual source. Therefore, the effective thermal injection velocity should be extracted at the source-channel barrier position [8].

$$\upsilon_{inj} = \frac{\sum_{i,j} N_{inv,i,j} \upsilon_{inj,i,j}}{\sum_{i,j} N_{inv,i,j}} \propto T^{\gamma_{\upsilon inj}},$$ (3-15)

where $N_{inv,i,j}$ was expressed as Eq. (3-2) and $\upsilon_{inj,i,j}$ is the injection velocity for i^{th} valley and j^{th} subband:

$$\upsilon_{inj,i,j} = \sqrt{\frac{2k_b T m_{ci}}{\pi m_{di}^2}} \frac{\mathfrak{J}_{1/2}(\frac{E_f - E_{ij}}{k_b T})}{\ln(1 + e^{\frac{E_f - E_{ij}}{k_b T}})},$$ (3-16)

where m_{ci} is the conductive effective mass for i^{th} valley, m_{di} is the density of state effective mass for i^{th} valley, E_f is the Fermi-level, E_{ij} is sub-band energy for i^{th} valley and j^{th} subband, and $\mathfrak{J}_{1/2}$ is the

Fermi-Dirac integral of order one-half. For two-fold valley, $m_{ci} = m_t$ and $m_{di} = m_t$ and for four-fold valley, $m_{ci} = \frac{2m_t m_l}{m_t + m_l}$ and $m_{di} = (m_t m_l)^{0.5}$. Here the longitudinal mass $m_l = 0.916 m_0$ and the transverse mass $m_l = 0.19 m_0$. The result has been shown in Fig. 3-11-1 and Fig. 3-11-2. It shows an increasing trend with temperature increasing and the temperature coefficient will increase with the channel length increasing.

Section 3.2.6 Inversion Carrier Density N_{inv} Extraction in Above Threshold Region ($V_G=0.8$ and $V_D=1mV/ 1V$)

With channel length scaling down to nanoscale, an important question we faced is the short channel effects. The short channel effects are attributed to two physical phenomena: (i) the limitation of the drift characteristic; and (ii) the variation of the threshold voltage. Here, we focus on the phenomenon (ii). This is the variation of the carrier density with channel length scaling down for each temperature. As shown in Fig. 3-12-1 and Fig. 3-12-2, the applied drain voltage will cause the channel carrier density decreasing at $L_G=90nm$ and $45nm$; and for $L_G=20nm$ and $15nm$, the channel carrier density increases due to the DIBL effect. Therefore, the temperature coefficient of the inversion carrier density β will vary with the channel length change. In the extraction of beta, there are two methods to do:

$$\beta_e = \frac{\Delta Q_{inv}}{Q_{inv}\Delta T}; \qquad\qquad\qquad (3\text{-}17)$$

$$\beta_{th} = \frac{\Delta V_{th}}{(V_G - V_{th})\Delta T}. \qquad\qquad\qquad (3\text{-}18)$$

Furthermore, DIBL is not a constant for any gate voltage as shown

in Fig. 3-6-2. It complicates the status of channel with the varying applied gate voltage. Therefore, we focus on the above threshold region and use the maximum transconductance method to extract V_{th} now. Result is shown in Fig. 3-12-4. Beta appears to slightly increase with channel length decreasing.

Section 3.2.7 Temperature Coefficient of Drain Current in Saturation Region ($V_G = 0.8V$ and $V_D = 1V$)

The temperature coefficient of drain current α is the most important factor. It represents the combination of all the effects. Therefore, it should be the same as the result of the combination of each factor. Fig. 3-13-1 shows the same characteristic as Fig. 3-12-2. Here α can be expressed as:

$$\alpha_{Id} = \frac{\Delta I_D}{I_D \Delta T};\tag{3-19}$$

$$\alpha_{th} = \frac{\Delta V_{th}}{(V_G - V_{th})\Delta T}.\tag{3-20}$$

The extracted result is shown in Fig. 3-13-3. We find α_{Id} is smaller than α_{th}. This is because mobility has the higher value at low temperature. Therefore, in order to calculate the BR, α_{Id} is the best way to extract the real variation of drain current between three temperatures. Owing to the same reason as α_{Id}, β_e is used to calculate the BR.

Section 3.2.8 Verification of Temperature Coefficient Method

Like the derivation shown in section 2.3, differentiating Eq. (3-9) with respect to temperature is performed:

$$\frac{\partial I_D}{I_D \, \partial T} = \frac{\partial Q_{inv}(x)}{Q_{inv}(x) \, \partial T} + \frac{\partial \mu}{\mu \, \partial T} + \frac{\partial \nabla \Phi_f(x)}{\nabla \Phi_f(x) \, \partial T}.\tag{3-21}$$

The result of each differential term has been shown in section 3-3, 3-6 and 3-7. At the saturation region, we assume the third of the right-hand side of Eq. (3-11) term is zero and $\mu_{app} \propto \upsilon_{sat} = \upsilon_{sat,0}(\frac{300}{T})^{\upsilon_{sat,exp}}$. Therefore, we can derive Eq. (3-22) as:

$$\alpha = \beta - \upsilon_{sat,exp}/T. \tag{3-22}$$

Result is shown in Fig. 3-14. It suggests that using the temperature coefficient method is feasible and the accuracy is better than 50%.

Section 3.3 Extraction of Ballistic Ratio (BR)

In this section, we will directly extract BR from the drain current and compare it with the temperature coefficient method. As shown in Eq. (3-23), we calculate BR at saturation region and there are two terms, $Q_{inv}(x_{vs})$ and υ_{inj}, that should be calculated first:

$$\frac{I_{D,sat}}{W} = Q_{inv}\upsilon_{ox}, \text{where } \upsilon_{ox} = \upsilon_{inj}BR_{dir}. \tag{3-23}$$

In the experiment part, we can measure C-V characteristics to get the corresponding inversion carrier density $Q_{inv,avg}$. Traditionally, the measured result is the macroscopic average. But in the channel backscattering theory it is not. It represents the carrier density at the barrier high in channel. Therefore, in the following we will extract BR at $X=X_{vs}$. As shown in Fig. 3-15-1, BR is extracted at the virtual source; it seems to increase with channel length shrinkage. This result shows the reflection rate decreasing with channel length decreasing. Considering the

physical limit on saturation velocity, it must saturate at $V_{sat} = V_{ox}$: BR is about 0.75 and r_c is about 0.15 at room temperature. Replacing BR with λ and L_{kt}, we have

$$BR_\lambda = \frac{1-r_c}{1+r_c} = \frac{\lambda}{2L_{kT}+\lambda} = \frac{\frac{2kT\mu_0}{v_T}\frac{\mathfrak{J}_0(\eta_F)}{\mathfrak{J}_{-1}(\eta_F)}}{2L_{kT}+\frac{2kT\mu_0}{v_T}\frac{\mathfrak{J}_0(\eta_F)}{\mathfrak{J}_{-1}(\eta_F)}}. \tag{3-24}$$

As shown in Fig. 3-15-2, BR_λ is slightly larger than BR_{dir} for higher temperature and BR increases with channel length shrinkage for the two methods. Although they have the same characteristics, the difference between each temperature is not the same. Therefore, we can predict BR extracted from temperature coefficient method. As shown in Eq. (2-16), we can use the five temperature coefficients to extract BR_{TC}. Result is shown in Fig. 3-15-3 and it shows a nearly constant characteristic for each channel length. Furthermore, using the temperature coefficient set A assumed in [3] even shows a negative trend at $L_G=15nm/$ 20nm. The reason is caused by the error in the five coefficients. In the five coefficients, we could simply assume the error would occur on critical scattering length. Other coefficients have been defined clearly. Therefore, substituting Eq. (3-24) into (3-23), we have

$$L_{kTcal} = \frac{kT\mu_0(1-BR_{dir})}{BR_{dir}V_{inj}}. \tag{3-25}$$

The calculated critical scattering length is shown in Fig. 3-16-1. And according to the new γ_{Lktcal}, we can extract the new BR as shown in Fig. 3-16-2. As our anticipation, it shows similar characteristics as the result of direct calculation.

Chapter 4

Conclusion

In the study, we used TCAD simulator to predict the characteristic of DG nMOSFETs with channel length scaling down to nanoscale. Here, the most important issue is the high field velocity saturation. It causes the carrier mobility degradation for the even general applied measurement drain bias of 0.025V, and generates DIBL effect for channel length is smaller than 45nm. Therefore, we should measure the mobility at small enough drain bias like 1mV. But the mobility degradation effect still exists for the operation voltage. For this reason, Prof. Lundstrom, *et al*. at Purdue University brings up the channel backscattering theory. They used another concept to explain the velocity saturation effect. In the theory, they think the critical scattering length stems from the virtual source point to the point with kT potential drop, rather than the virtual source point. The result between the DD model and channel backscattering model has not too much difference. But as we used the temperature coefficient method to calculate BR, the slight difference in the critical scattering length causes a strong variation on the temperature coefficient γ_{LkT}. We could infer carriers would be scattered in a range larger than kT-layer for higher temperature and in smaller than kT-layer for lower temperature. However, the channel backscattering theory is a useful theory to explain why we would face the awkward situation with the channel length scaling down.

References

[1] A. Pirovano, A. Lacaita and A. Spinelli, "Two-dimensional quantum effects in nanoscale MOSFETs," *IEEE Trans. Electron Devices*, vol. 49, no. 1, pp25-31, Jan. 2002.

[2] M. S. Lundstrom, "Elementary scattering theory of the Si MOSFET," *IEEE Electron Device Letters*, vol. 18, no. 7, pp. 361-363, July 1997.

[3] M. J. Chen, H. T. Huang, K. C. Huang, P. N. Chen, C. S. Chang and C. H. Diaz, "Temperature dependent channel backscattering coefficients in nanoscale MOSFETs," in *IEEE IEDM Tech. Dig.*, pp. 39-42, 2002.

[4] D. M. Caughey and R. E. Thomas, "Carrier mobilities in Silicon empirically related to doping and field," *Proc. IEEE*, pp. 2192–2193, Dec. 1967.

[5] M. J. Chen and L. F. Lu, "A parabolic potential barrier-oriented compact model for the k_bT layer's width in Nano-MOSFETs," *IEEE Trans. Electron Devices*, vol. 55, no. 5, pp. 1265-1268, May 2008.

[6] A. Rahman and M. S. Lundstrom, "A compact scattering model for the nanoscale Double-Gate MOSFET," *IEEE Trans. Electron Devices*, vol. 49, no. 3, pp. 481-489, March 2002.

[7] D. Vasileska, D. K. Schroder and D. K. Ferry, "Scaled silicon MOSFET's: Part II - Degradation of the total gate capacitance," *IEEE Trans. Electron Devices*, vol. 44, no. 4, pp. 584-587, April 1997.

[8] F. Assad, Z. Ren, D. Vasileska, S. Datta and M. Lundstrom, "On the performance limits for Si MOSFETs: a theoretical study," *IEEE Trans. Electron Devices*, vol. 47, pp. 232-240, Jan. 2000.

[9] M.Zilli, P.Palestri, D.Esseni and L.Selmi, "On the experimental determination of channel back-scattering in nanoMOSFETs," in *IEEE IEDM Tech. Dig.*, pp. 105-108,

2007.

[10] V. Barral, T. Poiroux, J. Saint-Martin, D. Munteanu, J. Autran and S. Deleonibus, "Experimental investigation on the Quasi-ballistic transport: Part I—determination of a new backscattering coefficient extraction methodology," *IEEE Trans. Electron Devices*, vol. 56, no. 3, pp. 408-419, March 2009.

[11] V. Barral, T. Poiroux, D. Munteanu, J. Autran and S. Deleonibus, "Experimental investigation on the Quasi-ballistic transport: Part II—backscattering coefficient extraction and link with the mobility," *IEEE Trans. Electron Devices*, vol. 56, no. 3, pp. 420-430, March 2009.

[12] K. Natori, "Ballistic metal-oxide-semiconductor field effect transistor," *J. Appl. Phys.*, vol. 76, pp. 4879–4890, 1994.

[13] D. J. Frank, S. E. Laux and M. V. Fischetti, "Monte Carlo simulation of a 30 nm Dual-Gate MOSFET: how short can Si go?," in *IEEE IEDM Tech. Dig.*, pp. 553-556, 1992.

[14] K. Banoo and M. S. Lundstrom, "Electron transport in a model Si transitor," *Solid- State Electronics*, vol. 44, issue 9, pp. 1689-1695, Sep. 2002.

Fig. 1-1 Schematic illustration of DG MOSFET.
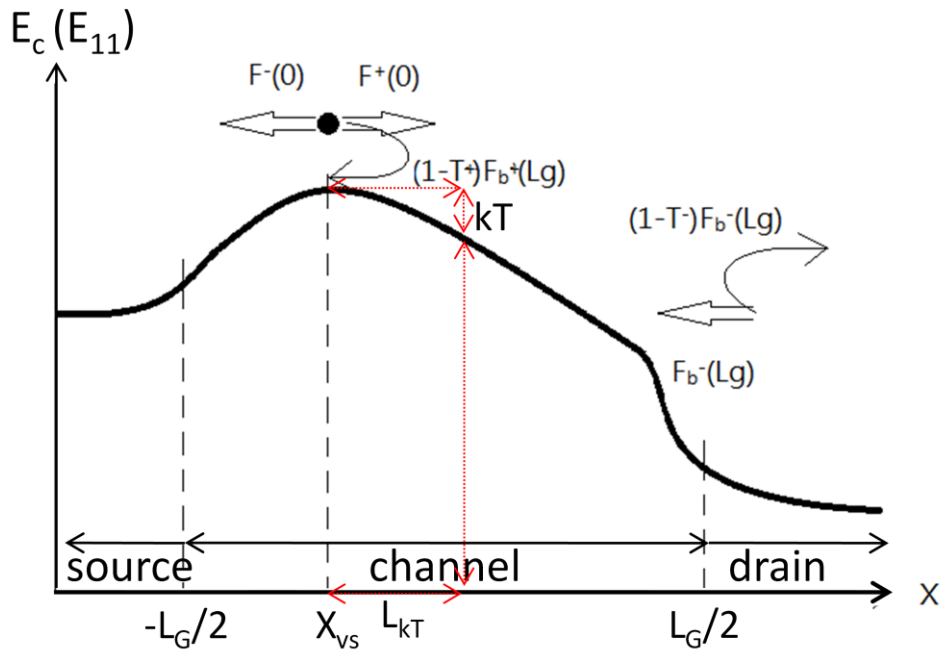
Fig. 1-2 Schematic illustration of channel backscattering theory in terms of the conduction band profile. F^+: the incident flux from the source is located at the peak of the source-channel barrier. F_b^-: the incident flux from the drain. T: the transmission coefficient for the flux cross the barrier for both directions.
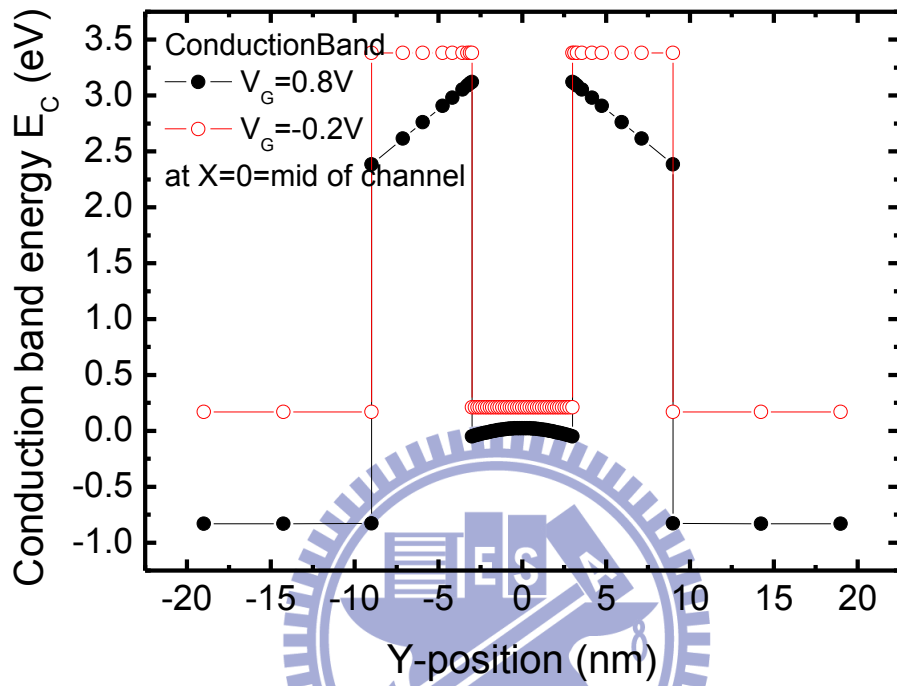
Fig. 3-1 The conduction energy band diagram along Y-sirection.

T=300K, V_D=0V, V_G=-0.2V/ 0.8V and L_G=90nm.
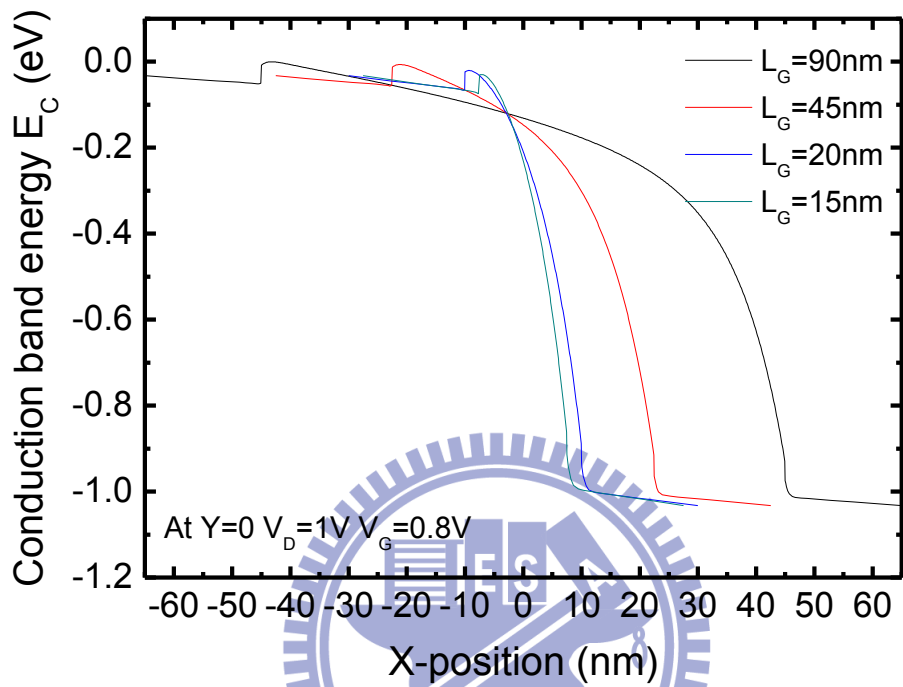
Fig. 3-2 The conduction energy band diagram along the channel.

T=300K, V_D=1V, V_G=1V and L_G=15/ 20/ 45/ 90nm.
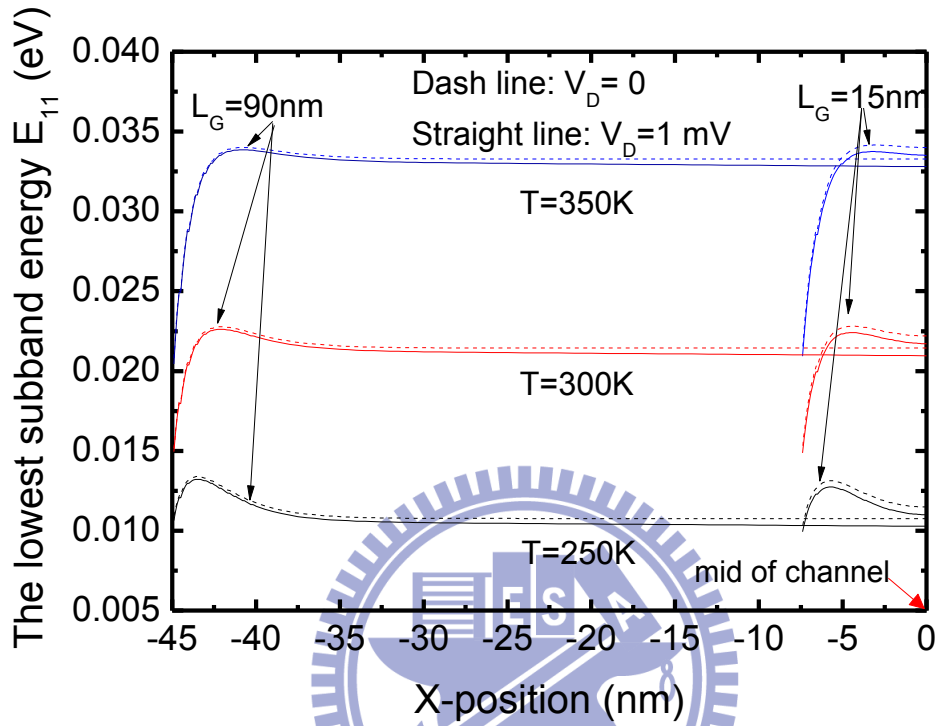
Fig. 3-3 The lowest subband E_{11} along the channel. T=250/ 300/ 350K, L_G=15/ 90nm and V_D=0/1mV. The difference between two different V_D is due to the variation of Fermi-level.
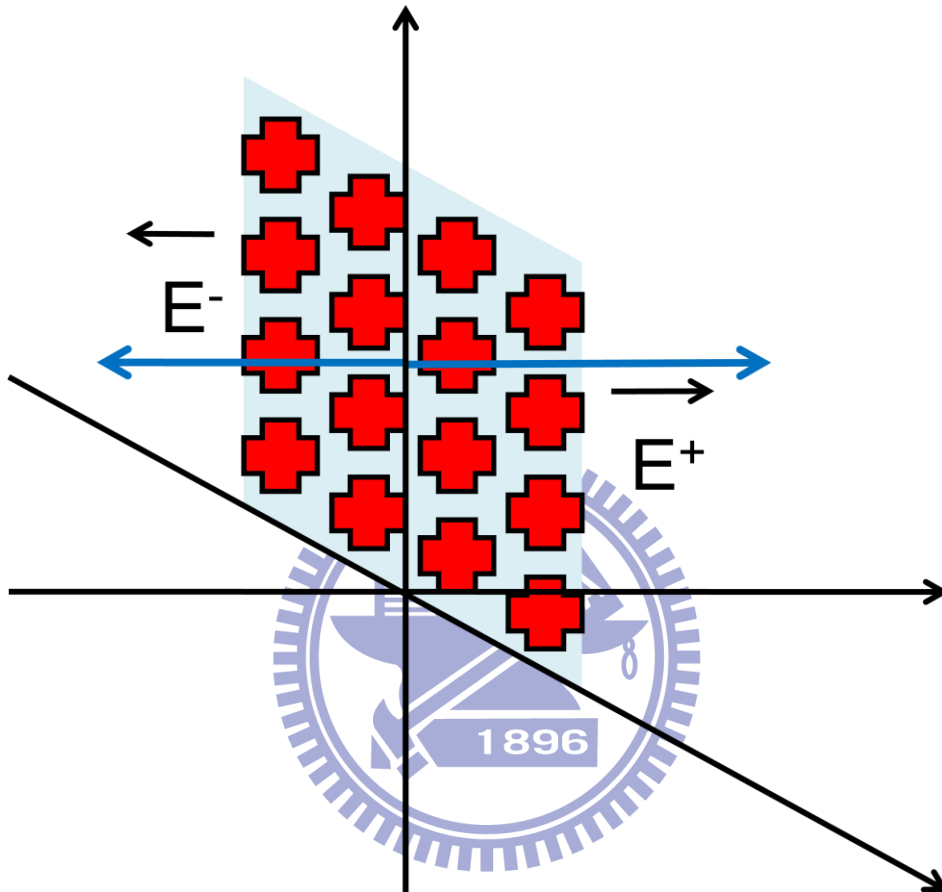
Fig. 3-4 Schematic diagram of sheet carriers.
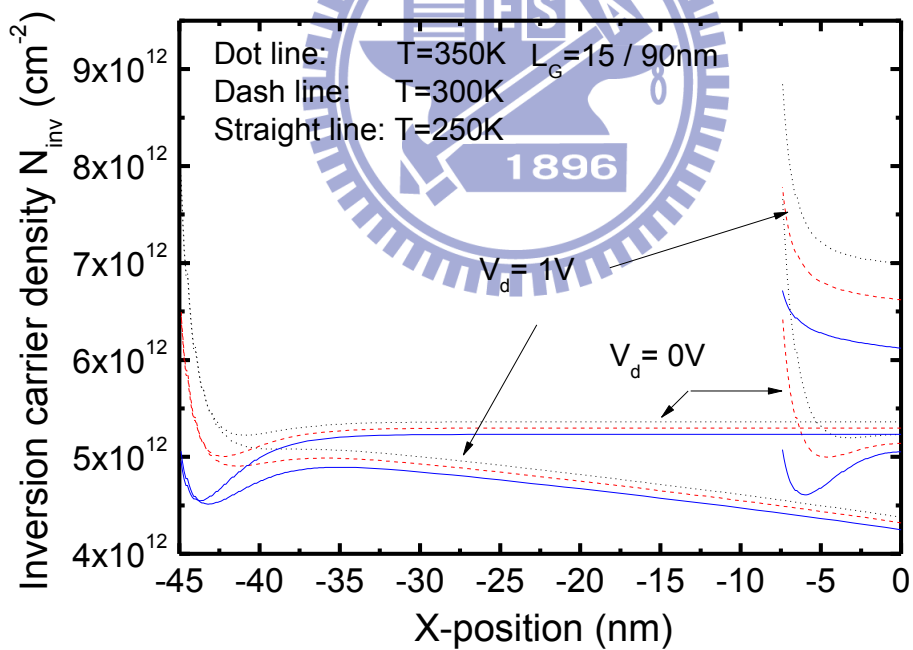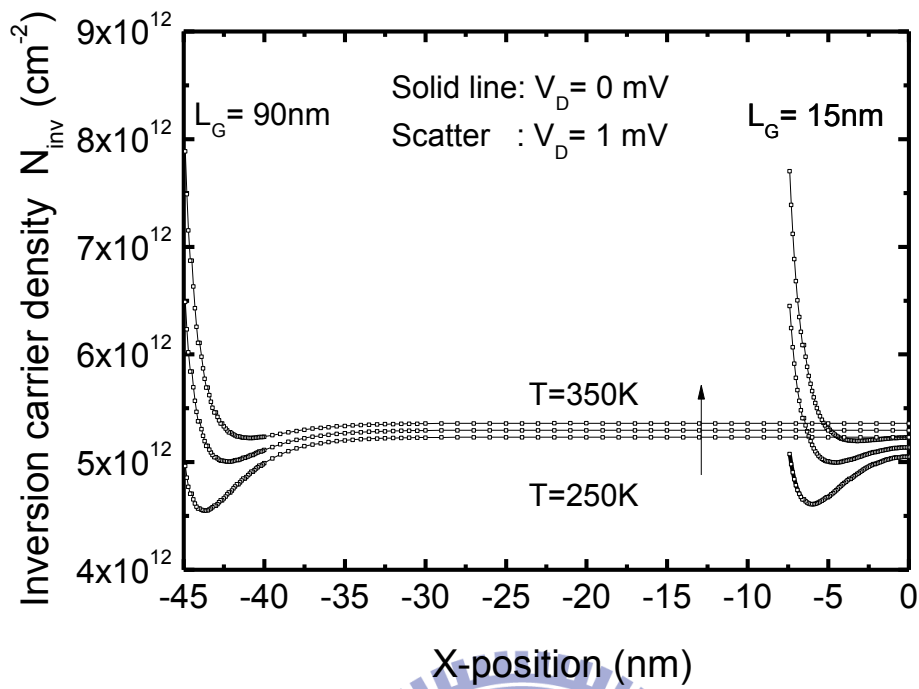
Fig. 3-5 The inversion carrier density, N_{inv} along the channel.

T=250/ 300/ 350K, L_G=15/ 90nm and V_D=0/ 0.001/ 1V.

DIBL gives arise in the carrier density increasing at L_G=15nm.
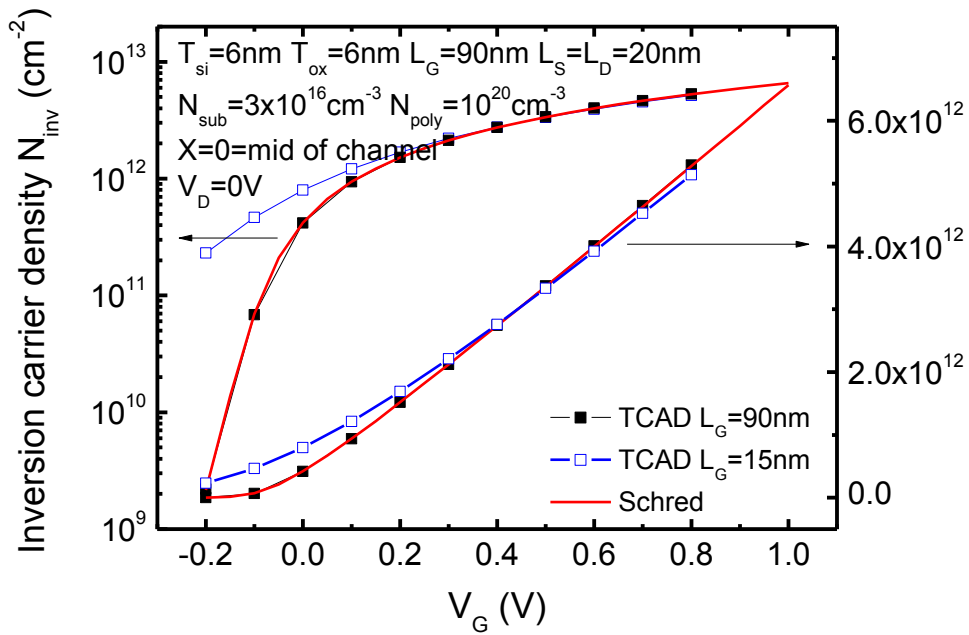
Fig. 3-6-1 The inversion carrier density N_{inv} for V_G=-0.2~1V at L_G=15/ 90nm, T=300K and V_D=0V of TCAD and Schred.
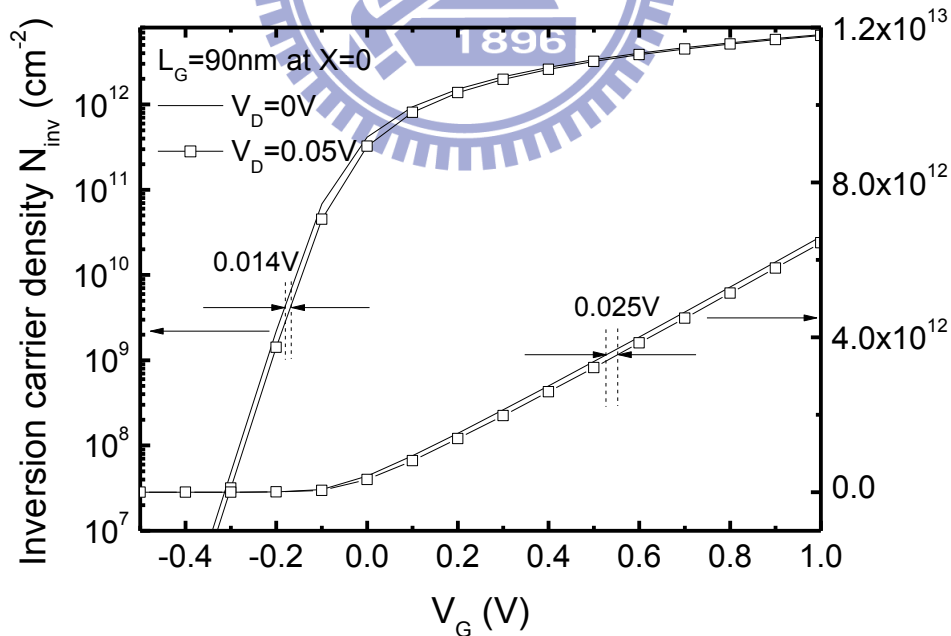
Fig. 3-6-2 The inversion carrier density N_{inv} for V_G=-0.5~1V at L_G=90nm, T=300K and V_D=0V/ 50mV.
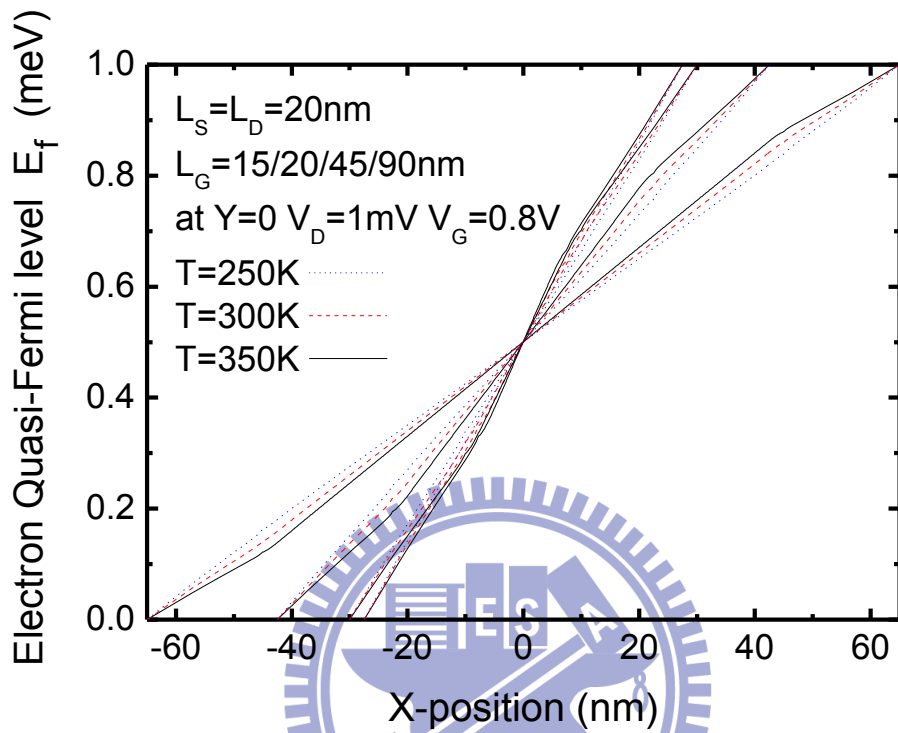
Fig.3-7 Electron Quasi-Fermi Level alone the channel for
L_G=15/ 20/ 45/ 90nm, V_D=1mV and V_G=0.8V at Y=0.
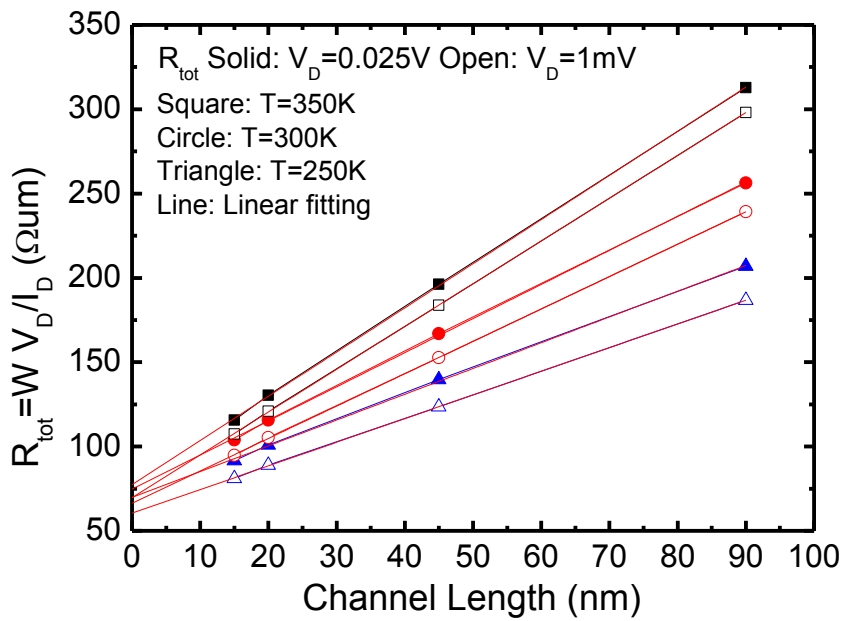
Fig.3-8-1 Total resistance for L_G=15/ 20/ 45/ 90nm at V_D=1mV/ 25mV and V_G=0.8V.
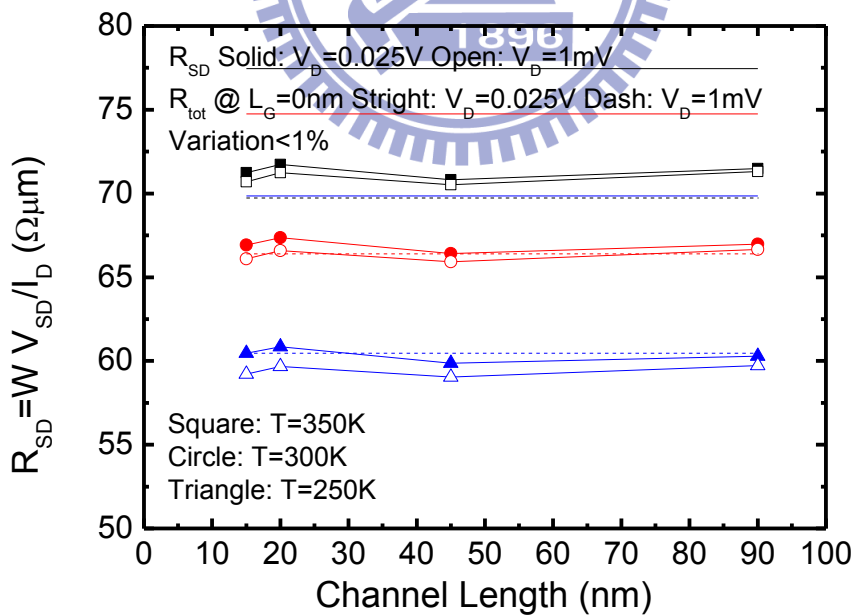
Fig.3-8-2 Source/ Drain resistance for L_G=15/ 20/ 45/ 90nm at V_D=1mV/ 25mV and V_G=0.8V.
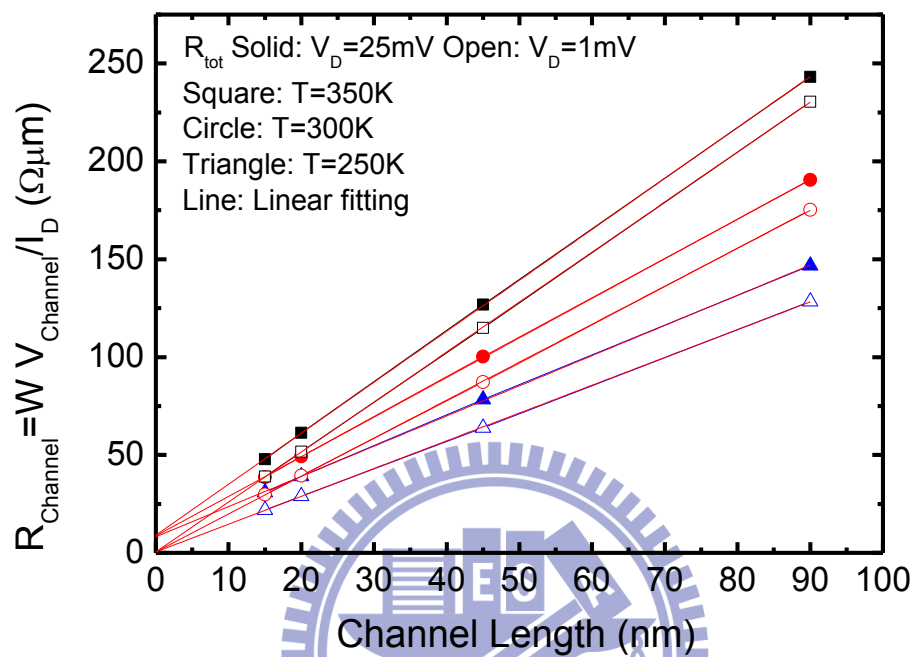
Fig.3-8-3 Channel resistance for L_G=15/ 20/ 45/ 90nm at V_D=1mV/ 25mV and V_G=0.8V.
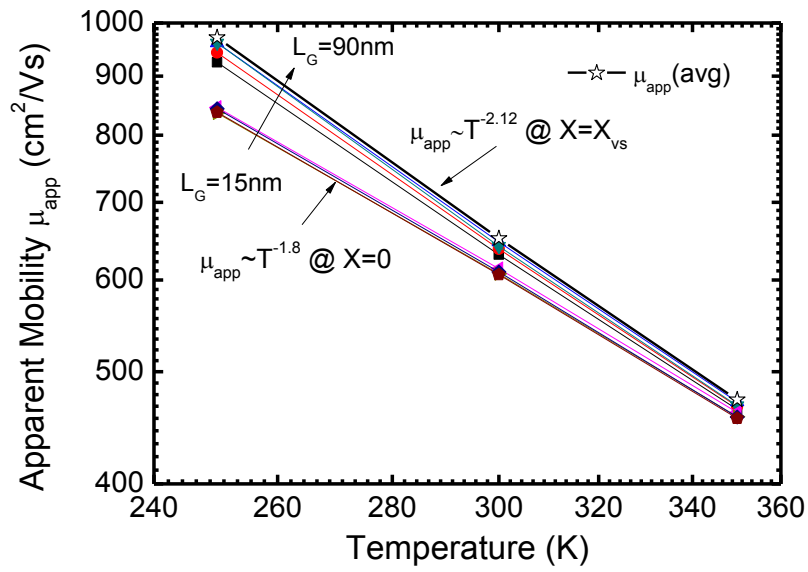
Fig. 3-9-1 The apparent mobility for L_G=15/ 20/ 45/ 90nm, T=250/ 300/ 350K and V_D=1mV.
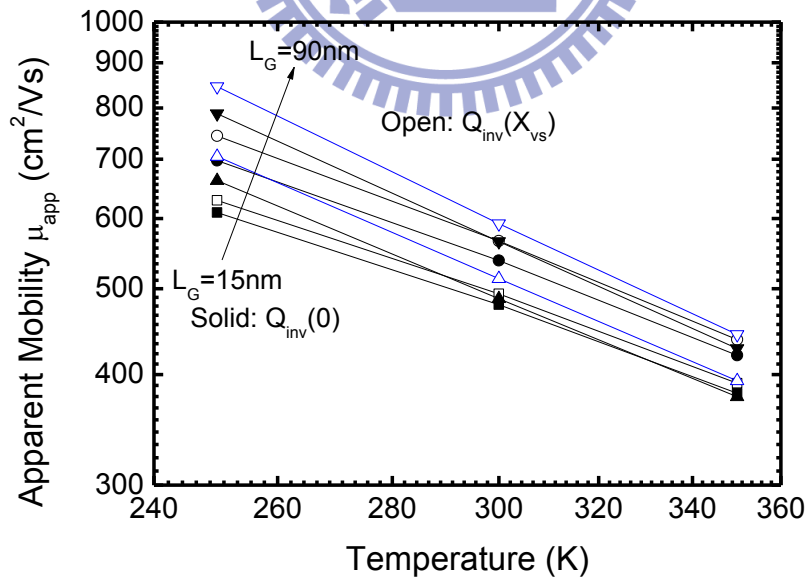
Fig. 3-9-2 The apparent mobility for L_G=15/ 20/ 45/ 90nm, T=250/ 300/ 350K and V_D=25mV.
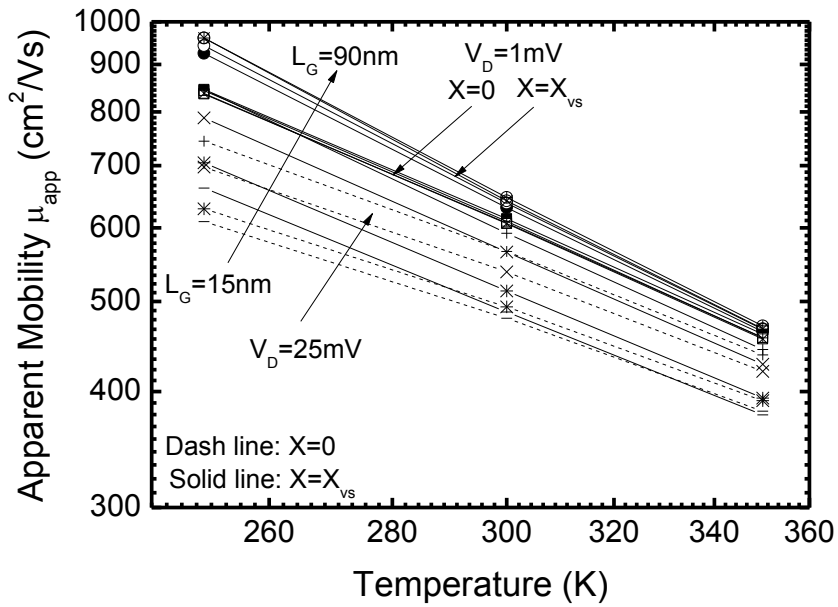
Fig.3-9-3 The apparent mobility for L_G=15/ 20/ 45/ 90nm,
T=250/ 300/ 350K and V_D=1/ 25mV.
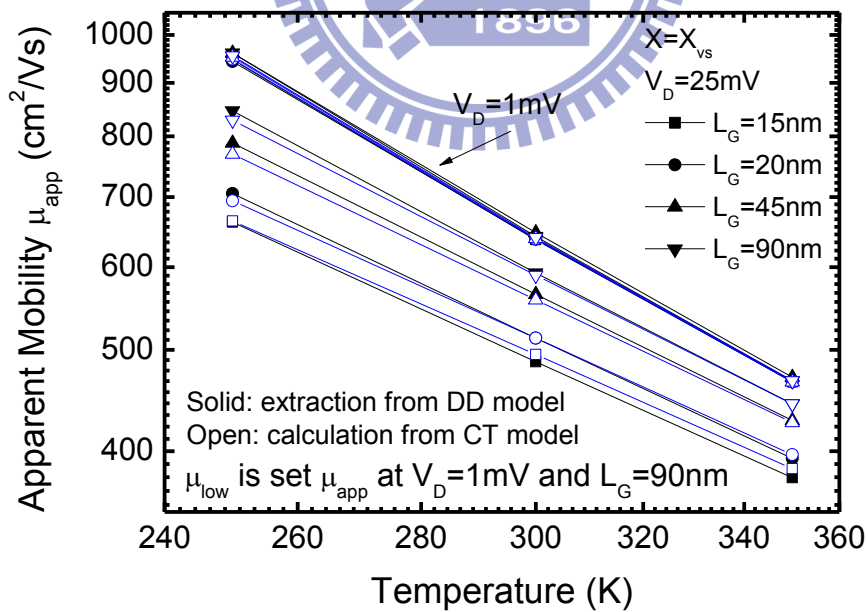
Fig.3-9-4 The apparent mobility extracted from DD model and
calculated from CT model.

Table 1 Caughey-Thomas formula parameters

Symbol	Parameter	Value	Unit
$\upsilon_{sat,0}$	vsat0	1.07×10^7	cm/s
$\upsilon_{sat,exp}$	vsatexp	0.87	1
β_0	beta0	1.109	1
βexp	betaexp	0.66	1
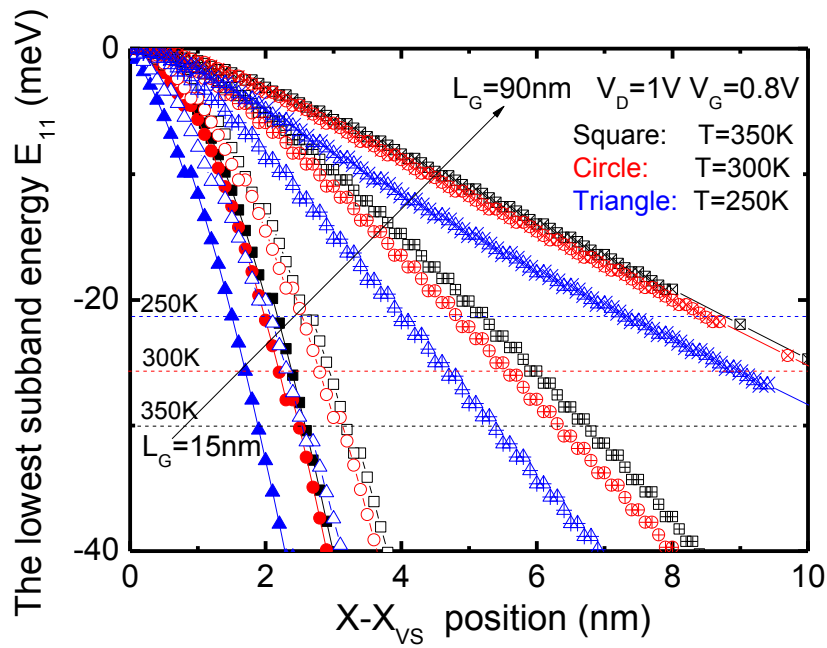
Fig 3-10-1. Profile of the lowest subband energy E_{11} at $V_G=0.8V$ and $V_D=1V$.
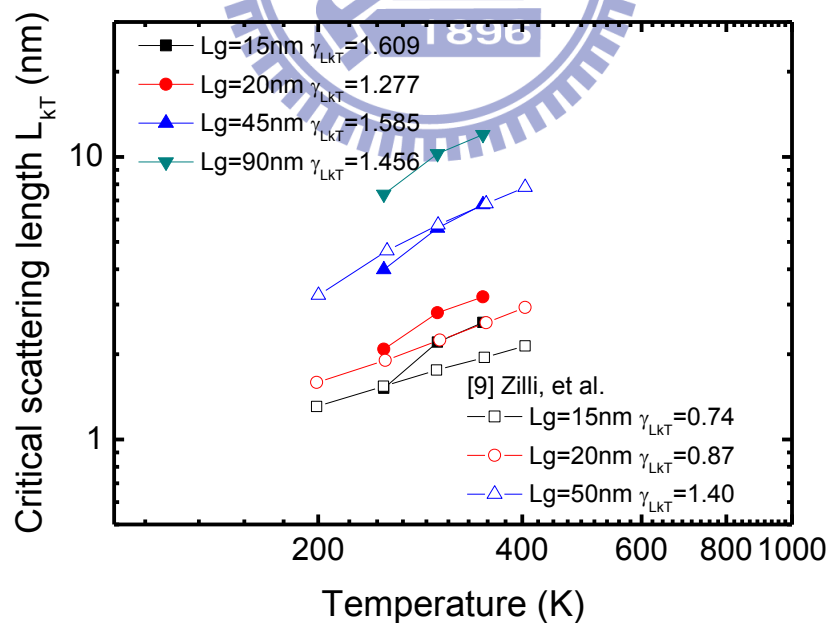
Fig 3-10-2. kT-layer extension as a function of the temperature at $V_G=0.8V$ and $V_D=1V$.
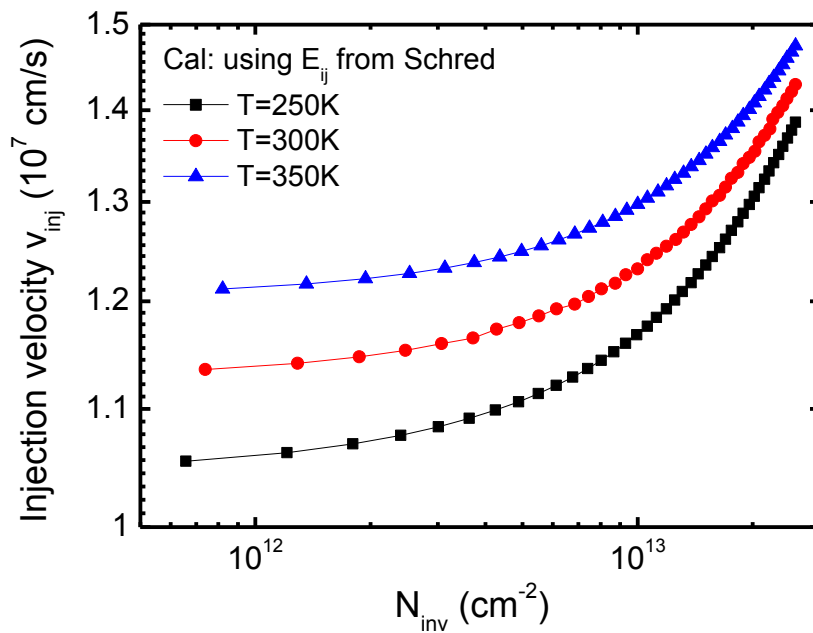
Fig 3-11-1. Injection velocity against the inversion carrier density for three temperatures.
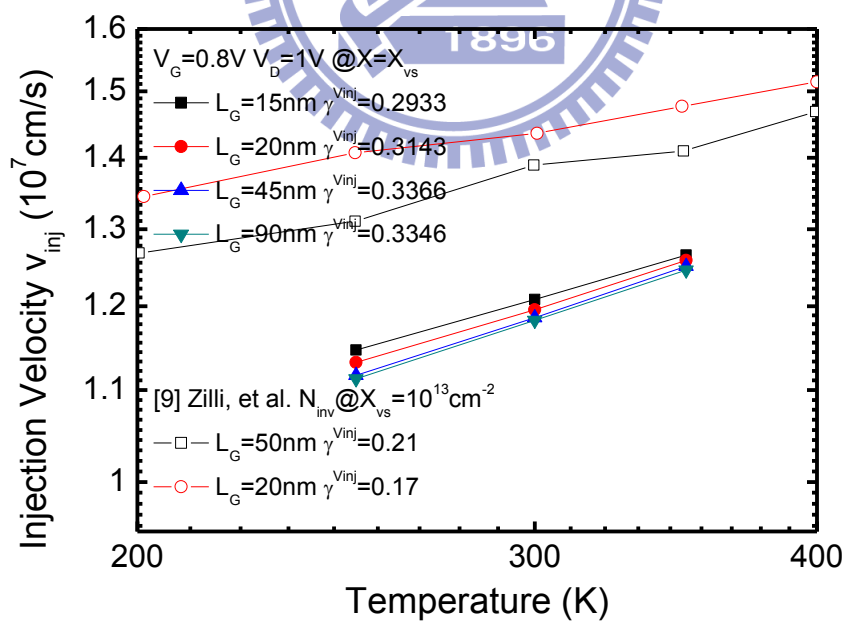
Fig 3-11-2. Injection velocity as a function of the temperature at V_G=0.8V and V_D=1V.
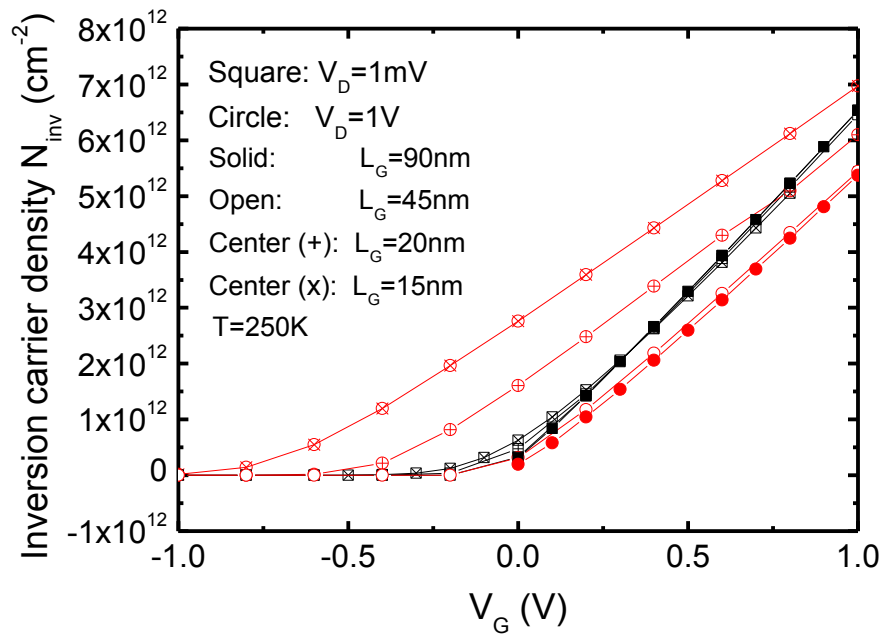
Fig 3-12-1. Inversion carrier density vs. V_G. At X=0 and T=250K.
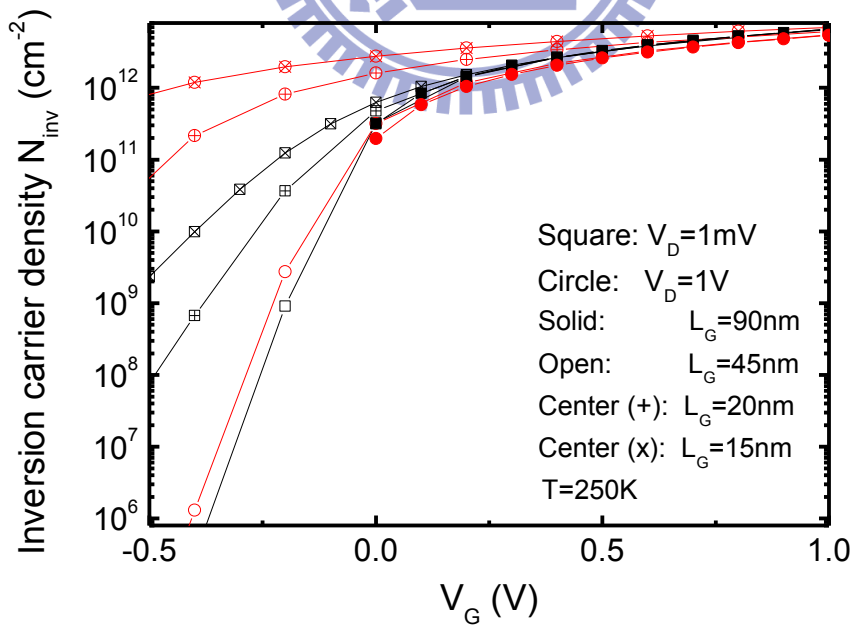
Fig 3-12-2. Inversion carrier density vs. V_G. At X=0 and T=250K.

40
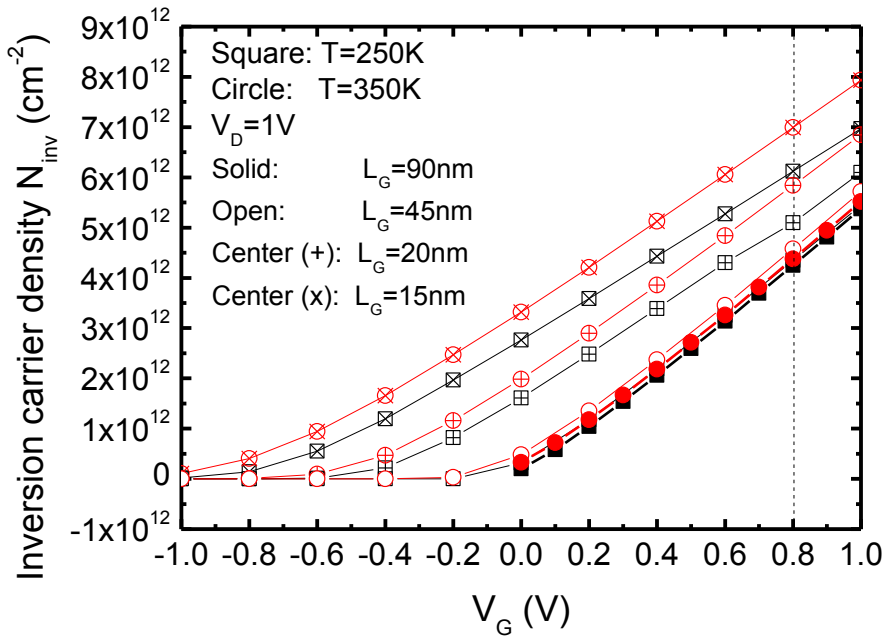
Fig 3-12-3. Inversion carrier density vs. V_G. At X=0 and V_D=1V.
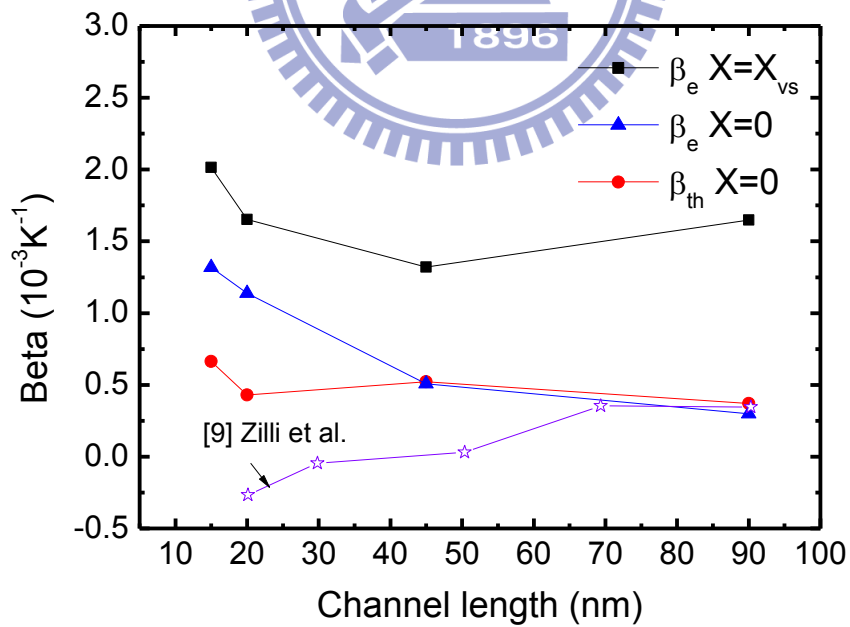
Fig 3-12-4. Beta for L_G=15/ 20/ 45/ 90nm, T=250/ 300/ 350K,
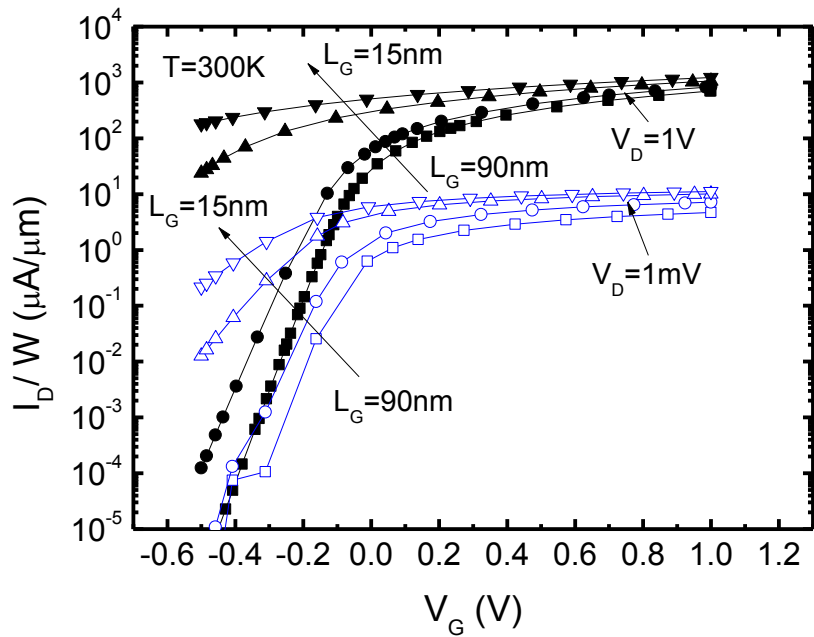
V_G=0.8 and V_D=1V.

Fig 3-13-1. Drain current vs. gate voltage.
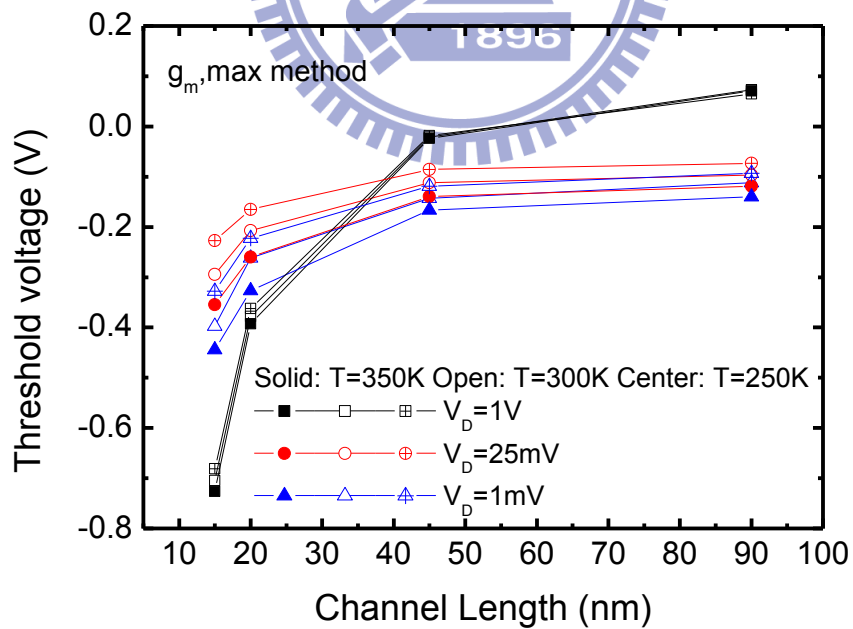
Fig 3-13-2. V_{th}-L_G. V_{th} was extracted by using the maximum transconductance method.
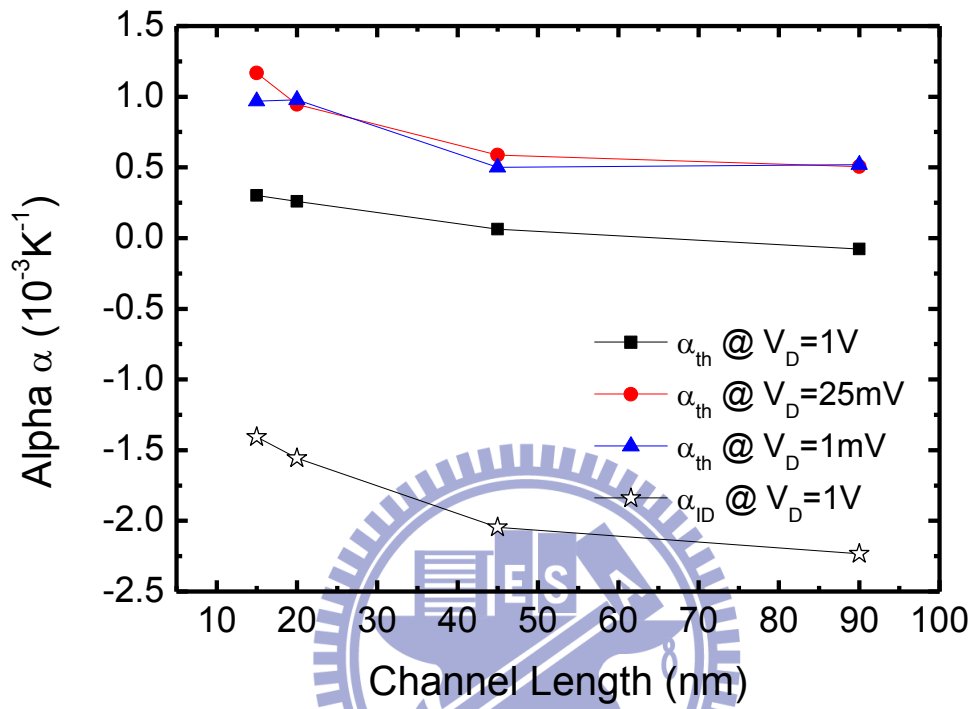
Fig 3-13-3. Alpha α against the channel length.
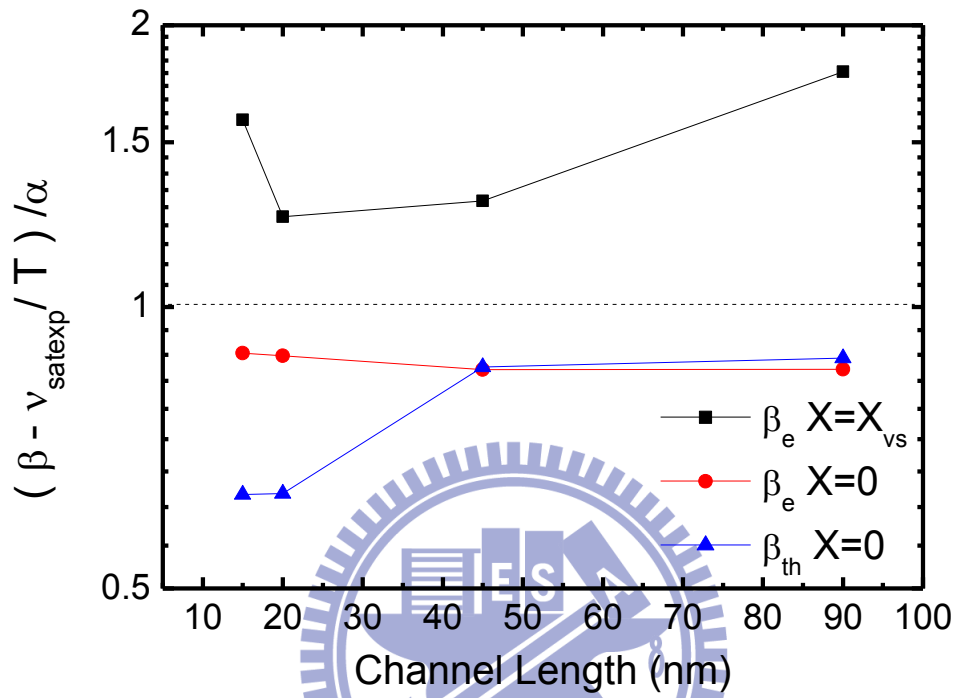
Fig 3-14. Ratio=$(\beta - \frac{v_{sat,exp}}{T})/\alpha$.
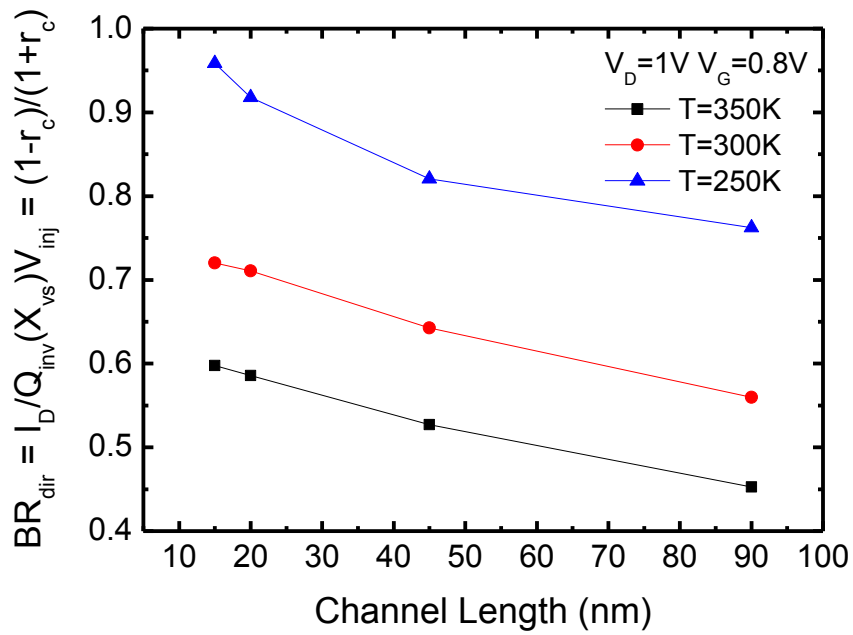
Fig. 3-15-1 BR for L_G=15/ 20/ 45/ 90nm, T=250/ 300/ 350K, V_G=0.8 and V_D=1V. BR increases with channel length scaling down.

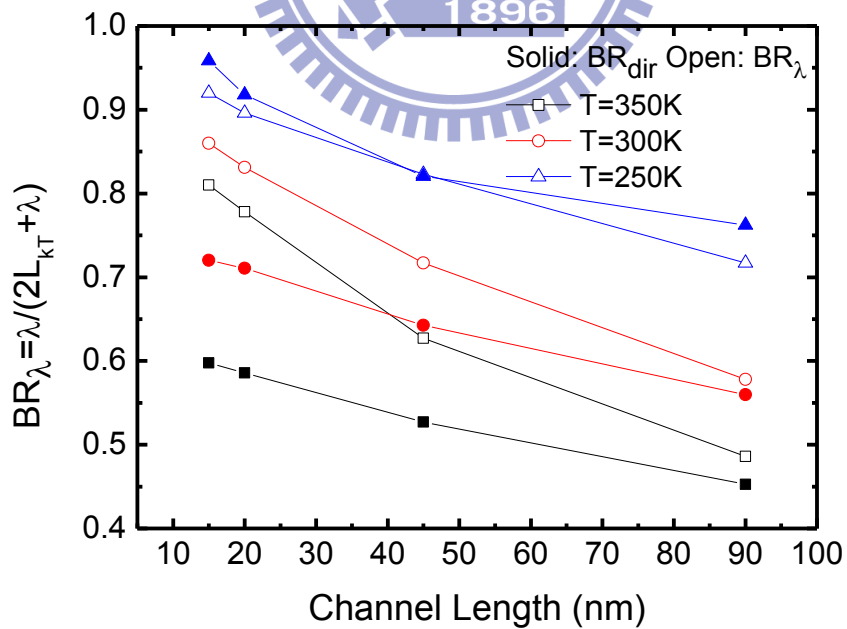Fig. 3-15-2 BR for L_G=15/ 20/ 45/ 90nm, T=250/ 300/ 350K, V_G=0.8 and V_D=1V. BR increases with channel length scaling down.
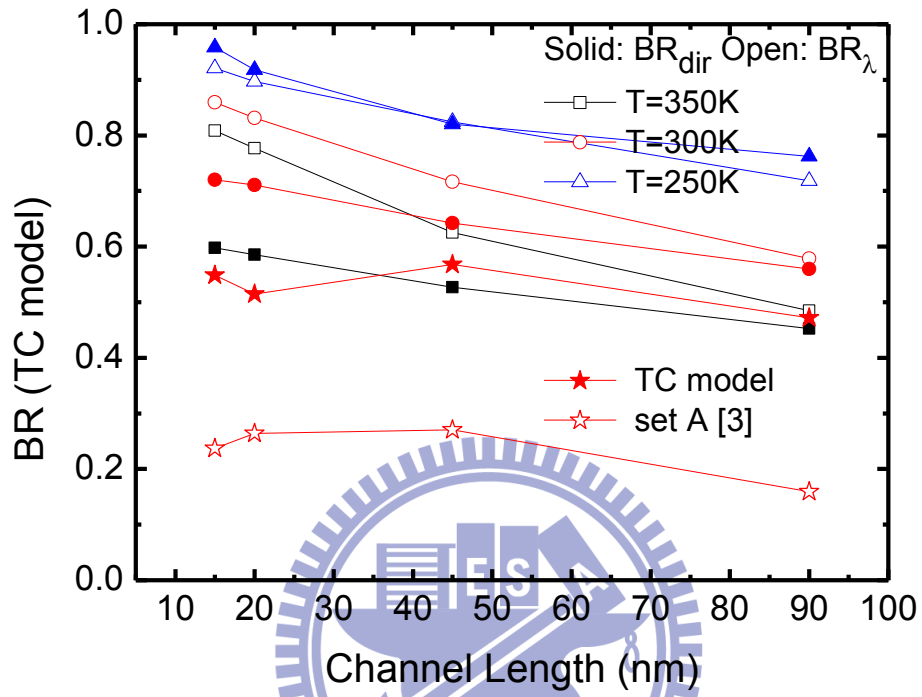
Fig. 3-15-3 BR (TC model) calculation.

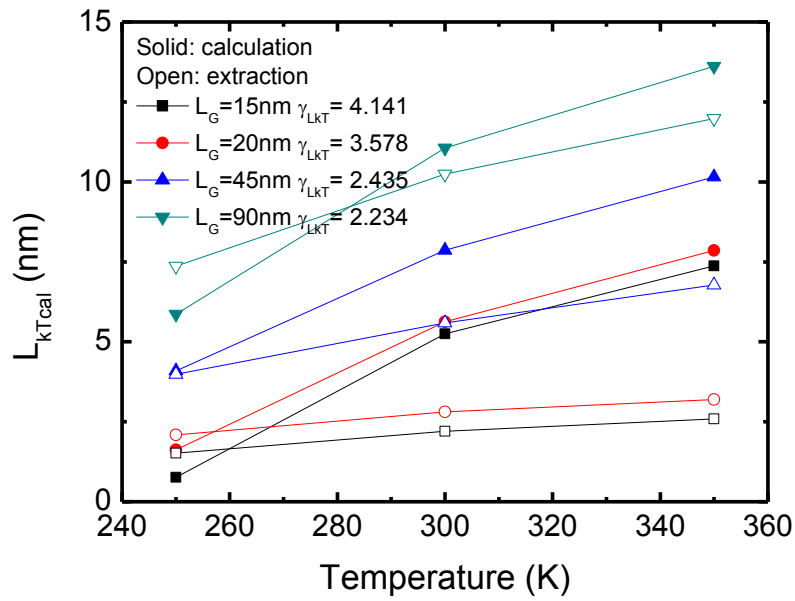Set A [3]: $\gamma_{Lkt} = 1$, $\gamma_{\mu} = -1.5$ and $\gamma_{\upsilon_{inj}} = 0.5$.

Fig. 3-16-1 The calculated L_{kTcal} versus temperature for different L_G, along with the extracted L_{kT}.
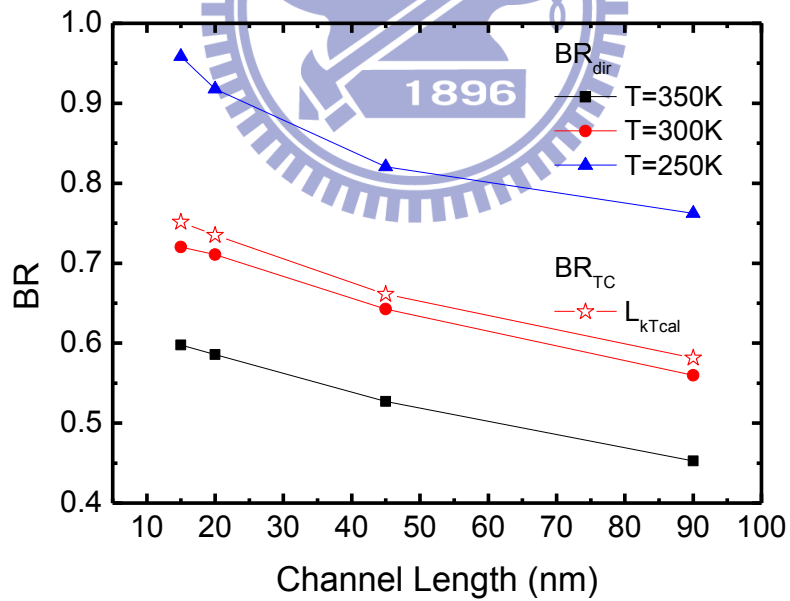

Fig. 3-16-2 The comparison of BR versus channel length for different temperature. BR_{TC} is also shown in the comparison of calculated L_{kT}.